

1 **Representation of the Autoconversion from Cloud to Rain Using a**
2 **Weighted Ensemble Approach: A Case Study Using WRF v4.1.3**

带格式的: 字体: (中文) +中文正
文 (宋体)

3
4 **Jinfang Yin^{1*}, Xudong Liang¹, Hong Wang², Haile Xue¹**

5
6 1 State Key Laboratory of Severe Weather (LaSW), Chinese Academy of
7 Meteorological Sciences (CAMS), Beijing 100081, China

8 2 Guangzhou Institute of Tropical and Marine Meteorology, China Meteorological
9 Administration (CMA), Guangzhou 510080, China

10
11 Submitted to *Geoscientific Model Development* (GMD)

12 On 5 July 2021

13
14 Corresponding to: Jinfang Yin (yinjf@cma.gov.cn)

15 **Abstract.** Cloud and precipitation processes remain among the largest sources of
16 uncertainties in weather and climate modeling, and considerable attention has been
17 paid to improve the representation of the cloud and precipitation processes in
18 numerical models in the last several decades. In this study, we develop a weighted
19 ensemble (named as EN) scheme by employing several widely used autoconversion
20 (ATC) schemes to represent the ATC from cloud water to rainwater. One unique
21 feature of the EN approach is that ATC rate is a weighted mean value based on the
22 calculations from several ATC schemes within a microphysics scheme with a
23 negligible increase of computation cost. The EN scheme is compared with the several
24 commonly used ATC schemes by performing real case simulations. In terms of
25 accumulated rainfall and extreme hourly rainfall rate, the EN scheme provides better
26 simulations than that by using the single Berry-Reinhardt scheme which was
27 originally used in the Thompson scheme. It is worth emphasizing, in the present study,
28 we only pay our attention to the ATC process from cloud water into rainwater with the
29 purpose to improve the modeling of the extreme rainfall events over southern China.
30 Actually, any (source/sink) term in a cloud microphysics scheme can be reated with
31 the same approach. The ensemble method proposed herein appears to have important
32 implications for developing cloud microphysics schemes in numerical models,
33 especially for the models with variable grid resolution, which would be expected to
34 improve the representation of cloud microphysical processes in the weather and
35 climate models.

删除的内容: a

带格式的: 非突出显示

删除的内容: s

删除的内容: dealt with

带格式的: 字体颜色: 红色, 非突出显示

带格式的: 非突出显示

删除的内容: of

40 1 Introduction

41 Cloud and precipitation processes and associated feedbacks have been confirmed to
42 cause the largest uncertainties in weather and climate modeling by the Intergovernmental
43 Panel on Climate Change (IPCC) ([Houghton et al., 2001](#)). Owing to the complex
44 microphysical processes in clouds and their interactions with dynamical and thermodynamic
45 processes, considerable attention has been devoted to developing cloud microphysics schemes
46 in the numerical weather and climate models in the last several decades, which is summarized
47 in several review [articles](#) (e.g., [Grabowski et al., 2019](#); [Khain et al., 2015](#); [Morrison et al.,](#)
48 [2020](#)). Because of fundamental gaps in the knowledge of cloud microphysics, however, there
49 are still a large number of empirical values derived and assumptions in microphysics schemes
50 based on limited observations, even from numerical simulations ([Tapiador et al., 2019](#)). As a
51 result, simulations are quite sensitive to microphysical parameter settings ([Falk et al., 2019](#);
52 [Freeman et al., 2019](#); [Gilmore et al., 2004](#)), and thus obvious differences occur frequently
53 from different simulations due to the poor representation of the empirical values and
54 assumptions ([Lei et al., 2020](#); [White et al., 2017](#)).

带格式的: 字体颜色: 红色, 非
突出显示

55 Collision-coalescence between cloud droplets forming [raindrops](#) is named as the
56 autoconversion (ATC), which is a significant microphysical process in warm clouds. Therefore,
57 [the](#) representation of the ATC from cloud water to rainwater is a key aspect of cloud
58 microphysical parameterization. Firstly, raindrop is initiated by ATC process in warm clouds,
59 which plays a significant role in the onset of a rainfall event. Besides, [the](#) ATC process has [an](#)
60 important influence on cloud microphysical properties by bridging aerosols, cloud droplets, and

带格式的: 字体颜色: 红色

删除的内容: i

删除的内容:

带格式的: 字体颜色: 红色

63 raindrops ([White et al., 2017](#)). Additionally, local circulation may be modified to a certain
64 extent due to [the](#) falling down of the initialized raindrops because of [the](#) terminal velocity of
65 [the](#) raindrop ([Doswell, 2001](#)). Moreover, changes in the rate of ACT had some effect on the
66 lower-tropospheric radiative flux divergence (Grabowski et al., 1999). Consequently, an
67 appropriate representation of the ATC process is helpful for our understanding of cloud micro-
68 and macro-properties, as well as precipitation processes.

69 Over the last several decades, much attention has been devoted to establishing ATC
70 schemes in atmospheric numerical models, and efforts are under way to create accurate and
71 computationally efficient ATC schemes. Kessler ([1969](#)) pioneered a simple scheme in which
72 the ATC rate was connected to cloud water content (CWC), and the scheme has been widely
73 used in bulk microphysics schemes (e.g., [Chen and Sun, 2002](#); [Dudhia, 1989](#); [Ghosh and Jonas,](#)
74 [1999](#); [Rutledge and Hobbs, 1984](#)). As an alternate way, Berry ([1968](#)) established a more
75 physical formulation in which not only CWC was considered but also cloud droplet number
76 concentration (N_c) and spectral shape parameter of cloud droplet size distribution. The Berry
77 scheme was featured by estimating the time t required for the sixth-moment diameter of the
78 spectral density to reach 80 μm by droplet coalescence, and Simpson and Wiggert ([1969](#))
79 increased the sixth-moment diameter to 100 μm . Ghosh and Jonas ([1999](#)) proposed a scheme
80 by combining the advantages of the Kessler and Berry schemes, which allow the use of the
81 simple linear Kessler-type expression and incorporating the effects of different cloud types. On
82 the other hand, several model-derived empirical schemes [were](#) established on the basis of
83 sophisticated microphysical simulations ([Berry and Reinhardt, 1974](#); [Franklin, 2008](#);
84 [Khairoutdinov and Kogan, 2000](#); [Lee and Baik, 2017](#)). Recently, Some studies (e.g., [Franklin,](#)

删除的内容: n

删除的内容: was

87 [2008](#); [Li et al., 2019](#); [Onishi et al., 2015](#); [Seifert et al., 2010](#)) the effect of turbulence on ATC
88 have been taken into account. Naeger et al. [\(2020\)](#) ~~proposed that~~ neglect of turbulence
89 influence within ~~an~~ ATC scheme resulted in very weak condensational and collisional growth
90 processes, and thus underpredicted the contribution of warm rain processes to the surface
91 precipitation. More recently, multi-moment schemes were explored, which appeared to
92 improve precipitation simulation ~~to~~ a certain extent ([Kogan and Ovchinnikov, 2019](#)).

删除的内容: a

删除的内容: in

删除的内容: of

93 To date, numerous ~~ATC~~ schemes have been established ([Beheng, 1994](#); [Berry, 1968](#);
94 [Berry and Reinhardt, 1974](#); [Caro et al., 2004](#); [Franklin, 2008](#); [Kessler, 1969](#); [Kogan and](#)
95 [Ovchinnikov, 2019](#); Lee and Baik, 2017; [Lin et al., 2002](#); [Liu and Daum, 2004](#); [Liu et al., 2006](#);
96 [Manton and Cotton, 1977a](#); [Seifert and Beheng, 2001](#); [Wood et al., 2002](#); [Yin et al., 2015](#)). As
97 were noted in previous studies ([Gilmore and Straka, 2008](#); [Hsieh et al., 2009](#); [Liu et al., 2006](#);
98 [Xiao et al., 2020](#); [Yin et al., 2015](#)), ATC rates predicted by different schemes can differ by
99 several orders of magnitude for a given CWC. Many previous studies have shown that ATC
100 rates are often overestimated/underestimated by those ATC schemes. For instance, Cotton
101 [\(1972\)](#) pointed out that ~~Kessler's~~ formulation produced the largest error at smaller CWCs, and

删除的内容: the

102 Berry's formulation consistently resulted in a low rain rate low in the simulated clouds.
103 Iacobellis and Somerville [\(2006\)](#) proposed that the Manton-Cotton parameterization ([Manton](#)
104 [and Cotton, 1977b](#)) produced much larger values of liquid water path (LWP) than
105 measurements both by satellites and surface-based at the Atmospheric Radiation Measurement
106 (ARM) Program's Southern U.S. Great Plains site. Silverman and Glass [\(1973\)](#) addressed
107 that the Cotton [\(1972\)](#) scheme resulted in a peak cloud water content ~~that occurred earliest in~~
108 ~~time at the lowest altitude but has the~~ lowest ~~value as~~ compared ~~with those~~ of the Kessler

删除的内容: that was in

删除的内容: in

删除的内容: , occurred earliest in time,
and occurred at the lowest height in
clouds,

删除的内容: to t

删除的内容: hose

120 | ([1969](#)) ~~and~~ Berry ([1968](#)) ~~schemes~~. However, Flatøy ([1992](#)) stated that Sundqvist's ([Sundqvist](#)
121 | [et al., 1989](#)) and Kessler's ([Kessler, 1969](#)) schemes gave comparable results when used a
122 | suitable choice of parameters. To the best of our knowledge, however, there is no one ATC
123 | parameterization scheme able to provide good results at all times so far, and much effort is
124 | necessary for further development of the ATC parameterization ([Michibata and Takemura,](#)
125 | [2015](#)).

删除的内容: ,

删除的内容: , and Simpson-Wiggert
(1969) schemes

126 | As noted by Morrison et al. ([2020](#)), one of the most serious issues of treating
127 | microphysics in weather and climate models is the uncertainties in the microphysical process
128 | rates owing to fundamental gaps in the knowledge of cloud physics. Posselt et al. ([2019](#))
129 | proposed that changes in cloud microphysical parameters produced the same order of
130 | magnitude change in model output as did changes to initial conditions, and thus it was
131 | important to constraint uncertainties in cloud microphysical processes if possible. Wellmann
132 | et al. ([2020](#)) also pointed out that model dynamical and microphysical properties were
133 | sensitive to both the environmental and microphysical uncertainties, and the latter resulted in
134 | larger uncertainties in the output of integrated hydrometeor mass contents and precipitation
135 | variables.

136 | There is still a poor representation of the ATC process in weather and climate models,
137 | and the potential uncertainties are non-negligible in the ATC schemes ([Michibata and](#)
138 | [Takemura, 2015](#)), and continued advancement of parameterizations ~~require~~ greater knowledge
139 | of the underlying physical processes in order to reduce the uncertainties, including from
140 | laboratory studies, cloud observations, and detailed process modeling ([Randall et al., 2019](#)).
141 | Most importantly, representing cloud processes consistently across multi-scales models with

删除的内容: are

146 | an empirical scheme appears to be one of the major challenges in cloud parameterizations
147 | ([Randall et al., 2019](#)). To fill this gap, the objective of this paper is to address how to reduce the
148 | negative effects of inherent uncertainties in the ATC (from cloud water to rainwater)
149 | parameterization within a cloud microphysics scheme to make the weather and climate models
150 | behave realistically. To achieve this goal, we design a weighted ensemble (herein abbreviated
151 | as EN) scheme to represent the ATC process by employing several widely used ATC schemes
152 | within a cloud microphysics scheme.

删除的内容: the

153 | This paper is organized as follows. An overview of the selected ATC schemes is presented
154 | in Section 2. Section 3 describes the approach of the ensemble scheme. The Weather Research
155 | and Forecasting (WRF) model configuration and experiment settings are given in Section 4.
156 | Simulated results of an extreme rainfall event are presented in Section 5. Finally, conclusions
157 | and discussions are given in Section 6.

158 | **2 Overview of the selected autoconversion schemes**

159 | In the present study, four widely used ATC schemes are selected, including Kessler ([1969](#))
160 | (KE) scheme, Berry and Reinhardt ([1974](#)) (BR) scheme, Khairoutdinov and Kogan ([2000](#))
161 | (KK) scheme, and Liu et al. ([2006](#)) (LD) scheme. Depending on the properties of the “bulk”
162 | microphysics schemes, the KE scheme is a one-moment scheme, and the BR and KK are
163 | double-moment schemes. The LD scheme provides a generalized expression with a smooth
164 | transition in the vicinity of the ATC threshold, which is featured by eliminating unnecessary
165 | assumptions inherent in the existing Kessler-type parameterizations. It should be noted it is
166 | still troublesome to justify in recommending one of the ATC schemes over the other, although

168 those schemes have been extensively tested and widely used in the previous studies ([Gilmore](#)
169 [and Straka, 2008](#); [Jing et al., 2019](#); [Michibata and Takemura, 2015](#); [White et al., 2017](#)).

170 2.1 Kessler (KE) scheme

删除的内容:

171 Kessler ([1969](#)) pioneered a simple expression in which ATC rate is related to CWC. The
172 KE scheme has been widely used in cloud-related processes in weather and climate numerical
173 models due to its simplicity. The ATC rate from cloud water to rainwater is expressed as

$$174 P_{ATC-KE}[\text{kg kg}^{-1} \text{s}^{-1}] = \rho_a \alpha (q_c - q_0) H(q_c - q_0) \begin{cases} q_c - q_0 \geq 0, H(q_c - q_0) = 1, \\ q_c - q_0 < 0, H(q_c - q_0) = 0. \end{cases} \quad (1)$$

175 where $\alpha = 0.001 \text{ s}^{-1}$ is a time constant, H is the Heaviside function, q_c is CWC in [the](#) unit of kg
176 m^{-3} , and ρ_a is air density. The threshold q_0 is the minimum CWC below which there is no
177 ATC from cloud water to rainwater (Fig. 1a). Owing to the simple and linear expression, the
178 KE scheme is computationally straightforward to implement in numerical models. However,
179 the major limitation of the KE scheme results in its inability to identify different conditions

180 such as maritime and continental clouds ([Ghosh and Jonas, 1999](#)). More [specifically, the KE](#)
181 [scheme only took CWC into account, while cloud number concentration was not incorporated,](#)

删除的内容:

182 [This may partially explain the KE scheme yielded the large errors at low CWC proposed by](#)
183 [Cotton \(1972\).](#) Besides, it is impossible to obtain the thresholds directly used in the scheme

带格式的: 超链接, 字体: (中文) Times New Roman, 字体颜色: 自动设置, 不检查拼写或语法

184 from observations at present, while cloud microphysical processes are sensitive to the
185 thresholds ([Plssett et al., 2019](#)). A modified Kessler scheme was proposed by Yin et al. ([2015](#))

带格式的: 超链接, 字体: (中文) Times New Roman, 不检查拼写或语法

186 in which q_0 is diagnosed as a function of altitude by using a CWC-height relationship which
187 was derived from CloudSat observations. In [order to get reasonable results](#), different values of
188 q_0 were chosen by various studies. For instance, a value of 0.5 g m^{-3} is given in Kessler's

删除的内容: fact

192 (1969), Reisner (1998), and Schultz (1995). Thompson (2004) reduced to a small value of
 193 0.35 g m^{-3} . Kong and Yau (1997) and Tao and Simpson (1993) gave a value of 2 g kg^{-1} , while
 194 a small value of 0.7 g kg^{-1} was assigned in Chen and Sun (2002). In this work, the same value
 195 of 0.5 g m^{-3} as that assigned in Kessler's (1969) is chosen.

196 2.2 Berry-Reinhardt (BR) scheme

197 Berry and Reinhardt (1974) proposed a physical formulation to represent the ATC process
 198 in clouds, which is given by

$$199 P_{ATC-BR} [\text{kg kg}^{-1} \text{ s}^{-1}] = \frac{2.7 \times 10^{-2} \rho_w q_c \left[\frac{1}{16} \times 10^{20} D_{mean}^4 (1 + \mu)^{-0.5} - 0.4 \right]}{\frac{3.7}{\rho_a q_c} \left[0.5 \times 10^6 D_{mean} (1 + \mu)^{-1/6} - 7.5 \right]^{-1}}. \quad (2)$$

200 Here, μ represents shape parameter of a gamma distribution, ρ_w is liquid water density. D_{mean}
 201 is the mean diameter (unit in m) of the total cloud droplets, which is computed from

$$202 D_{mean} = \left(\frac{6q_c}{\pi \rho_w N_c} \right)^{1/3}. \quad (3)$$

203 Here, π is the circumference ratio. The BR scheme was developed theoretically in which not
 204 only CWC but also cloud number concentration was incorporated. An important characteristic
 205 is that maritime and continental clouds can be differentiated by the BR scheme using different
 206 parameters (Simpson and Wiggert, 1969; Pawlowska and Brenguier, 1996). Cotton (1972)
 207 argued that the BR scheme seems to underestimate rain formation in their simulations.

208 Compared to KE, the BR scheme has treated the process more rigorously (Ghosh and Jonas,
 209 1999). It should be noted that ATC rates given by BR are quite sensitive to N_c (Fig. 1b).

210 2.3 Khairoutdinov-Kogan (KK) scheme

211 Khairoutdinov and Kogan (2000) proposed a computationally efficient and relatively

删除的内容: n

带格式的: 字体颜色: 红色

213 simple scheme, which aims at large-eddy simulation (LES). One of the advantages is that there
 214 is no need to define a threshold, and this scheme has been broadly used in numerical models
 215 (e.g., Morrison et al., 2009). The ATC rate is given by

$$216 \quad P_{ATC-KK} [\text{kg kg}^{-1} \text{s}^{-1}] = 1350 q_c^{2.47} (N_c \times 10^{-6})^{-1.79}. \quad (4)$$

217 The KK scheme uses a simple power law expression based on a series of large-eddy
 218 simulations. Generally speaking, the autoconversion rate increases with increasing CWC
 219 and/or decreasing cloud number concentration. The simple expression is a key advantage of the
 220 KK scheme, which makes it possible to analytically integrate the microphysical process rates
 221 over a probability density function (Griffin and Larson, 2013). In view of Fig. 1c, the KK
 222 scheme has a strong dependency on N_c . Increasing N_c from 100 to 500, ATC rates decrease,
 223 dramatically, especially at the CWCs over 1.0 g m^{-3} . Unlike other schemes, ATC is allowable
 224 in the KK scheme even with very low CWCs, which might lead to overestimations under such
 225 conditions.

删除的内容: bin microphysical calculations

带格式的: 字体颜色: 红色

删除的内容: s

删除的内容: the KE

226 2.4 Liu-Daum-McGraw-Wood (LD) scheme

227 A generalized ATC parameterization was proposed by Liu et al. (2006). The approach
 228 improved the representation of the threshold function by applying the expression for the critical
 229 radius derived from the kinetic potential theory. The parameterization is given by

$$230 \quad P_{ATC-LD} [\text{kg kg}^{-1} \text{s}^{-1}] = \kappa \beta^6 q_c^3 N_c^{-1} \{1 - \exp[-(1.03 \times 10^{16} N_c^{-3/2} q_c^2)^\mu]\}. \quad (5)$$

231 Here, $\kappa (= 1.1 \times 10^{10} \text{ kg}^{-2} \text{ m}^3 \text{ s}^{-1})$ is a constant. β is a parameter related to the relative dispersion ε
 232 of cloud droplets, which is obtained from

$$233 \quad \beta = \left[\frac{(1+3\varepsilon^2)(1+4\varepsilon^2)(1+5\varepsilon^2)}{(1+\varepsilon^2)(1+2\varepsilon^2)} \right]^{\frac{1}{6}}. \quad (6)$$

238 Here, a value of 0.5 is assigned to ε following Liu et al. (2006). The LD scheme assumes that
239 autoconversion rate is determined by CWC, cloud number concentration, and relative
240 dispersion of cloud droplets. Xie and Liu (2015) suggested that the LD scheme considering
241 spectral dispersion was more reliable for improving the understanding of the aerosol indirect
242 effects, compared to the KE and BR schemes. Note that, the LD scheme is characterized by
243 the smooth transition in the vicinity of the ATC threshold.

带格式的: 字体颜色: 红色

删除的内容: T

244 3 Description of the ensemble (EN) scheme

245 As has been mentioned above, ATC rates predicted by different schemes can differ by
246 several orders of magnitude for a given CWC. Nowadays, it is still troublesome to judge which
247 scheme is preferred to others at all times ([Ghosh and Jonas, 1999](#); [Jing et al., 2019](#); [Liu et al.,](#)
248 [2006](#); [Michibata and Takemura, 2015](#)). To the best of our knowledge, each one has its own
249 advantages and disadvantages. Keeping this fact in our mind, we propose a weighted the EN
250 scheme by employing the above-listed four commonly used ATC schemes, and the weighted
251 ensemble ATC rate (P_{ATC-EN}) is given by

$$252 P_{ATC-EN} [\text{kg kg}^{-1} \text{s}^{-1}] = \frac{w_{KE} P_{ATC-KE} + w_{KK} P_{ATC-KK} + w_{LD} P_{ATC-LD} + w_{BR} P_{ATC-BR}}{w_{KE} + w_{KK} + w_{LD} + w_{BR}}. \quad (7)$$

253 Here, w_{xx} , referring to that for KE, KK, LD, and BR, respectively, is the weight of each ATC
254 scheme. It is worth noting that Eq. (7) is easily reduced into any single scheme form by setting
255 all w_{xx} values of 0 except for one of them. Therefore, it is a flexible way to use any one or more
256 schemes to calculate P_{ATC-EN} by adjusting w_{xx} . Of course, it is also convenient to reduce the
257 effect of any one of them by giving a small value of w_{xx} . At present, the same weights with the
258 value of 1.0 are assigned for all schemes for simplicity. Note that, the weights can be

删除的内容: y

261 modulated according to weather conditions. One of the features of the EN scheme is that the
262 weighted mean is calculated within a microphysics scheme, and the increase of computation
263 cost is negligible.

删除的内容: increasing

264 Similar to an ensemble prediction system ([Lewis, 2005](#)), the EN scheme is expected to
265 reduce the potential uncertainties from the use of any ATC scheme alone under various CWC
266 conditions. For example, no cloud water converts into rain water in the KS scheme when the
267 cloud water is less than the threshold, while in the KK scheme it always occurs. However, the
268 KS scheme has much higher ATC rates owing to the linear relationship (Eq. 1), compared to
269 those of the KK scheme. Most importantly, the EN scheme is beneficial for the multi-scale
270 numerical weather and climate modeling systems, especially for variable resolution models
271 (e.g., the Model for Prediction Across Scales, MPAS ([Skamarock et al., 2012](#)), the
272 Global-to-Regional Integrated forecast SysTem, GRIST, ([Zhang et al., 2019](#))), because it is
273 flexible to represent cloud processes consistently across all model scales under the various
274 conditions. Depending on grid distance, one or more schemes can be used independently in a
275 variable resolution model. For example, we assign all w_{xx} to 0 except for w_{KK} in the fine grid
276 distance region, and a mean value from the calculation of two or more schemes is utilized in
277 the grid distance transition zone.

删除的内容: subgrid-scale

278 To facilitate comparisons among the aforementioned ATC schemes, an idealized
279 experiment is performed with a wide range of CWCs in the calculations. A rough value of N_c is
280 set to 300 cm^{-3} in the continental clouds (e.g., Hong and Lim, 2006; Thompson et al., 2008).
281 For convenience, air density is approximately fixed at $1.29 \times 10^{-3} \text{ g cm}^{-3}$ here. It is noteworthy
282 that the value of 2 is assigned to μ for both BR and LD schemes. Figure 2 compares the EN

删除的内容: ly

286 scheme with the selected four schemes with a wide range of CWCs from 0.01 to 1.0 g m⁻³. One
287 can see that all the schemes yield ATC rates of ~10⁻⁹ g cm⁻³ s⁻¹, although there are significant
288 discrepancies among the different schemes. For the KS scheme, the ATC of cloud water to rain
289 water does not start until the CWC exceeds the threshold q_0 (Eg. 1). In contrast, the other
290 schemes are allowable even given fair low CWCs.

291 | Comparatively speaking, both KS and LD predicts a larger ATC rate than the other ATC
292 schemes (the BR or KK scheme) for a given CWC. As for the former group, LD yields the
293 largest ATC rate with CWC below 0.6 g m⁻³, while KS generates the largest ATC with CWC
294 over 0.6 g m⁻³. Wood and Blossey (2005) argued that the ATC rate defined in LD would give
295 the total rate of mass coalescence among cloud droplets and is typically much larger than the
296 true ATC rate. With N_c fixed at 300 cm⁻³, the BR scheme shows close ATC rates to those of KK.
297 Note that the KK scheme, originally developed for the Large Eddy Simulation (LES) model,
298 yields the lowest ATC rate, followed by the BR scheme. The EN scheme provides a similar
299 pattern to LD, but nearly half ATC rates of those are yielded by the latter. It should be
300 emphasized that ATC rates are fairly sensitive to N_c (Fig. 1), and a higher or lower N_c would
301 cause great changes.

删除的内容: ly

302 **4 Simulations of an extreme rainfall event**

303 **4.1 Overview of the rainfall event**

304 An extreme rainfall event hit Guangzhou megacity in the early morning hours of 7 May
305 2017. Within 18 hours (during the period of 2000 Beijing standard time (BST, BST = UTC +
306 8) 6 May to 1400 BST 7 May), there were 12 rain gauge stations over 250 mm during the

308 rainfall process. The spatial distribution of the rainfall appears two heavy rainfall cores over
309 Jiulong (JL) and Huashan (HS) regions (Fig. 3a). The event was featured by the heaviest
310 rainfall in Guangzhou megacity over the past six decades with the maximum total amount of
311 542 mm within 18 hours at JL station (Fig. 3a). It also broke the record of 3-h accumulated
312 rainfall amount with the value of 382 mm. Another marked feature of this rainfall event was its
313 extreme hourly rainfall rate of 184 mm h⁻¹, which is the second-highest over the Guangdong
314 Province, China. The hourly rainfall rate is comparable to the highest value of 188 mm h⁻¹
315 observed at Yangjiang station in Guangdong Province on 23 June 2013.

316 4.2 Model configuration and experiment settings

317 This event was well simulated and investigated by Yin et al. (2020), focusing on the
318 effects of urbanization and orography. The WRF model configurations, and initial and
319 boundary conditions are the same as Yin et al. (2020) except for updating to the
320 WRF-ARW(v4.1.3) model (Skamarock et al., 2019) with several minor bugs fixed. For
321 convenience, an overview of the WRF model configures is presented here. The triple nested
322 domains have x, y dimensions of 313×202, 571×334, and 862×541 with grid sizes of 12, 4,
323 and 1.33 km, respectively. The WRF model physics schemes are configured with the
324 Thompson microphysics scheme (Thompson et al., 2008) with the modifications of ATC
325 parameterization, the rapid radiative transfer model (rrtm) (Mlawer et al., 1997) for both
326 shortwave and longwave radiative flux calculations, the Yonsei University (YSU) planetary
327 boundary layer (PBL) scheme (Hong et al., 2006), the MM5 Monin-Obukhov scheme for the
328 surface layer (Janjić, 1994), and the Noah-MP land-surface scheme (Niu et al., 2011). The Kain
329 cumulus parameterization scheme (Kain, 2004) is utilized for the outer two coarse resolution

删除的内容: second

删除的内容: .

332 domains, but being bypassed in the finest domain. All the three nested domains of the WRF
333 model are integrated for 18 hours, starting from 2000 BST 06 May 2017, with outputs at 6-min
334 intervals. The initial and outermost boundary conditions are interpolated from the National
335 Centers for Environmental Prediction (NCEP) Global Forecast System 0.25 degree re-analysis
336 data at 6-h intervals. In order to introduce realistically the UHI effects of the Guangzhou
337 metropolitan region, the Four-Dimension Data Assimilation (FDDA) functions are activated
338 ([Reen, 2016](#)) by performing both the surface observation nudging and the analysis nudging
339 from 2000 BST 6 to 0800 BST 7 May 2017. Please refer to Yin et al. ([2020](#)) for more details
340 about the model configuration.

341 As has been addressed above, it is convenient to ~~conduct~~ a simulation with any of the
342 ~~above-listed~~ ATC schemes alone. In total, two experiments were carried out with the EN and
343 BR schemes. It should be noted that the BR scheme was used originally in the Thompson
344 scheme, and the EN ~~was~~ newly coupled into the Thompson scheme in this work.

删除的内容: launch

删除的内容:

删除的内容: were

带格式的: 字体颜色: 红色

345 5. Results

346 5.1 Spatial distribution of accumulated rainfall

347 Figure 3 compares the spatial distribution of 18-h simulated total rainfall from the
348 simulations with the EN and BR schemes to the observed. Generally speaking, both schemes
349 are able to capture ~~the~~ main characteristics of the extreme rainfall event. One can see that the
350 simulated rainfall amount compares favorably to the observed both at HS and JL, although the
351 JL storm has a 10-15 km eastward location shift. Yin et al. ([2020](#)) argued that the location
352 errors may be related to large-scale meteorological conditions. Comparatively speaking, the

删除的内容: the

删除的内容: at

358 EN and BR schemes performed better than others. The two centralized rainfall cores over HS
359 and JL were successfully captured by the EN and BR schemes, with the simulated heaviest
360 rainfall amount of 537 mm and 569 mm, respectively (Fig. 3b,c). As for the EN scheme (Fig.
361 3b), the simulated 18-h total rainfalls were 320 mm and 537 mm over HS and JL, respectively,
362 which was close to the observations of 341 mm and 542 mm (Fig. 3a). Similarly, the BR
363 scheme performed equivalently to the EN scheme, with the maximum rainfall of 347 mm and
364 569 mm over Huashan and Jiulong regions, respectively (Fig. 3c). Note that the simulated
365 heaviest over the Huashan region were comparative among each other. In view of the results,
366 we will compare the maximum hourly rainfall rates near JL from the simulations of the EN
367 and BR schemes to that of observations in the next sections. It should be noted the results in
368 the present study are a little better than (or equivalent to at least) those in Yin et al. (2020)
369 because of the update of the WRF version4.1.3 model with some improvements in dynamical
370 framework and bug fixes.

删除的内容: observed

371 5.2 Evolution of the simulated hourly rainfall

372 Figure 4 shows the observed and simulated time series of hourly maximum rainfall rates
373 over the Jiulong region. The observed peak rainfall near JL occurred at 0600 BST 7 May with
374 the hourly rates of 184 mm hr⁻¹. However, the simulated peak rainfall from the EN scheme took
375 place at 0700 BST 7 May, which was about 1 h later than the observed, with the hourly rates of
376 151 mm hr⁻¹. As for the BR scheme, the simulated peak rainfall rate occurred two hours later,
377 with the value of 144 mm hr⁻¹. As a matter of fact, both EN and BR schemes under-predicted
378 the peak hourly rainfall rate near JL. It is worthy to note that the observed timings of initiating
379 and ending of the extreme rainfall production episode, i.e., near 0300 and 1000 BST 7 May,

删除的内容: ER

382 | respectively, were reproduced successfully. However, both simulated peak rates occurred later
383 | than the observed due to the slower increases in rain-producing rates than the observed. More
384 | specifically, the observed hourly rate increased from about 16 mm hr⁻¹ to 184 mm hr⁻¹ just in
385 | one hour (i.e., from 0500 to 0600 BST). However, the simulated from the EN scheme increased
386 | from 0.3 mm hr⁻¹ at 0400 BST to about 79 mm hr⁻¹ at 0600 BST, and then to 151 mm hr⁻¹ at
387 | 0700 BST 7 May. As for the simulated with the BR scheme, it increased from 2 mm hr⁻¹ at 0400
388 | BST to about 104 mm hr⁻¹ at 0700 BST, and then to 144 mm hr⁻¹ at 0800 BST 7 May. One
389 | unique feature of the observations was the rapid increase of the hourly rainfall rate. The rainfall
390 | produced by the EN scheme peaked within 2 h while the BR scheme peaked over a period of 4
391 | h. Additionally, both the simulated rainfall rates decrease for several hours. Generally speaking,
392 | the EN scheme performed much closer to the observed, compared to that of the BR scheme.
393 | Note that the longer heavy rainfall period from the BR scheme contributed partially to the
394 | over-prediction of the 18-h accumulated rainfall (Fig. 3c).

395 5.3 Evolutions of radar reflectivity

396 | In view of the performance of the accumulated rainfall and the maximum hourly rainfall
397 | rates, we only compare the radar reflectivity from the simulations with the EN scheme to the
398 | results of the BR scheme. Figure 5 exhibits the structures and evolutions of convective cells
399 | over JL region by comparing the simulated composite radar reflectivity to the observed. The
400 | first well-organized radar echo formed near 0000 BST over the Huashan region (not shown),
401 | which was located at the northern edge of a surface high- θ_e (equivalent potential temperature)
402 | tongue with significant convergence. As the southeasterly flow moved slowly eastward and the
403 | cold outflows resulted from previous convection, the Huashan storm dissipated while the storm

删除的内容: the

删除的内容: observed

删除的内容: over a period of

带格式的: 字体颜色: 红色

407 began to develop over the Jiulong region, both in its size and in intensity (Fig. 5a). The storm
408 rapidly intensified during the period from 0430 to 0530 BST, with the peak reflectivity beyond
409 55 dBZ near the leading edge (Fig. 5a,b). The Jiulong storm moved fairly slowly, keeping more
410 or less quasi-stationary shortly after its formation (Fig. 5a-c). Both the quasi-stationary nature
411 and intense radar reflectivity explain the extreme rainfall production rate occurring at JL during
412 the 1-h period of 0500 - 0600 BST. Subsequently, the Jiulong storm weakened, but its
413 associated peak radar reflectivity still remained over 50 dBZ, which was consistent with the
414 continued generation of significant rainfall near JL until 0800 BST (Fig. 4).

415 It is obvious that both the EN and BR schemes captured the development of the Jiulong
416 storm, with the main features that were similar to the observed, including quasi-stationary
417 nature, southeastward expansion, and concentrated strong radar reflectivity during the extreme
418 rainfall stage. Both simulations successfully generated a lower- θ_e pool with a distinct outflow
419 boundary interacting with the moist southeasterly flow near the ground. It should be noted that
420 the initiation and organization of both simulated Jiulong storms were about 1.7 h later than the
421 observed, and it occurred at a location nearly 10-15 km kilometers to the east of the observed
422 one. Generally speaking, both simulations with the EN and BR schemes produced extreme
423 rainfall amounts close to those observed and their spatial distributions agree well with
424 observations.

425 In terms of the spatial distribution of radar reflectivity, similar patterns can be seen
426 between the EN and BR schemes in the early stage before 0712 UTC, while differences are
427 visible at the extreme rainfall stage (Fig. 5e,h). One can find that the Jiulong storm simulated
428 with the EN scheme (Fig. 5f) developed more rapidly than that from the BR scheme, almost 1

删除的内容: the

删除的内容: the

431 h earlier than the latter (Fig. 5i). This was consistent with the timing lag in the hourly extreme
432 rainfall production (Fig. 4). Clearly, the ACT process has an important influence on the
433 convective development of deep convection associated with the extreme rainfall producing
434 within the Jiulong storm, which will be explored in view of the cloud microphysical processes
435 in the next section.

436 5.4 The Effects on Macro- and Micro-physical Processes

437 The spatial distribution of hourly rainfall, and temporal-averaged surface temperature
438 and horizontal wind during the period from 0600 BST to 0700 BST from the simulations with
439 the EN and BR schemes are displayed in Fig. 6. As has been stated above, the total rainfall
440 shows a slight difference between EN and BR over the Jiulong region (Fig. 3b,c). In view of
441 the spatial distribution of the hourly rainfall during the period (i.e., 0600 BST to 0700 BST 7)
442 when maximum hourly rainfall occurred (Fig. 6), the EN scheme generated larger rainfall area
443 and stronger rainfall rate than those of the BR scheme, although both schemes produced
444 similar spatial distribution patterns in rainfall area, and temporal-averaged surface
445 temperature and horizontal wind filed. The result was consistent with the idealized
446 experiments given in Fig. 2. For a given CWC, the EN scheme had a larger ATC rate,
447 compared to the BR scheme, and the difference becomes obvious with the increase of CWC.
448 Consequently, the EN scheme produced more rain water of small- to middle size, compared to
449 the BR scheme. The larger rain water was favorable for the coalescence of large precipitation
450 particles from the upper levels, which made the larger contribution to the extreme rainfall rate.
451 This is why the EN scheme produced larger rainfall than the BR scheme. The result was

删除的内容: maximum

删除的内容: a

删除的内容: a

删除的内容: increasing

带格式的: 字体颜色: 红色

删除的内容: The ATC process mostly occurred at lower levels, resulting in a higher number concentration of small raindrops (Duan et al., 2020).

删除的内容: The higher number concentration of middle-size raindrop was favorable for the coalescence of large precipitation particles from the upper levels, which made the larger contribution to the extreme rainfall rate (e.g., Bao et al., 2019). As a result, the EN scheme produced larger rainfall than the BR scheme.

469 consistent with Fu and Lin (2019) in which temporal and spatial extent of the “vigorous rain
470 formation region” where most of the rain was produced. Those features can also be viewed
471 from the vertical sections in Fig. 7. One can see that the largest radar reflectivity reaches the
472 ground, like a bell on the ground (Fig. 7a). This unique feature was reported by Li et al. (2020)
473 based on the observations from the S-band dual-polarization radar at Guangzhou station,
474 Guangdong Province, China. The bell-shaped radar reflectivity was consistent with the
475 episode of the extreme hourly rainfall. The strong radar reflectivity mainly resulted from
476 raindrops coalescence owing to the higher number concentration raindrop in the lower levels
477 (Bao et al., 2020). That is to say, collecting rain water by the collision-coalescence process at
478 the lower levels helped create a large rainfall rate at the ground. As for the BR scheme (Fig.
479 7b), a middle-level radar reflectivity core was obvious above nearly 1 km up to 4 km,
480 indicating that raindrops coalescence occurred intensively between those levels and
481 evaporation of raindrops was significant below 1 km. The evaporation near above the surface
482 was a considerable factor abating the surface rainfall rate. In view of the vertical distribution
483 of radar reflectivity, the EN scheme generated a maritime-like convective storm, whereas the
484 convective storm simulated by the BR scheme was close to a continental-like convection. It
485 should be noted that except for evaporation, large particle (raindrop) breakup can lead
486 reflectivity values to decrease toward the surface because reflectivity is much sensitive to
487 raindrop size. In the present case, the evaporation of raindrops was remarkable. However, a
488 slight difference was found in differential reflectivity Zdr in the lower levels, indicating that
489 large particle (raindrop) breakup was weak.

490 Both the EN and BR schemes provide tilted storms in view of vertical cross from south to

删除的内容: .

删除的内容: The t

删除的内容: the

带格式的: 字体颜色: 红色

删除的内容: s

带格式的: 字体颜色: 红色

删除的内容: That is to say, the latter
have a smaller number of raindrops
near the surface.

498 north through the extreme rainfall. During this episode, the updraft was dominant in the storm,
499 and a weak downdraft occurred in the lower levels at the back of the convective storm.
500 Besides, both EN and BR reproduced very close thermal patterns in terms of potential
501 temperature. Note that the EN scheme had a slightly weaker updraft than that of the BR
502 scheme, although only make the modifications in the ATC parameterization in the
503 microphysics scheme (Fig. 7a,b), suggesting that change in cloud microphysical processes can
504 lead to some variations in dynamical processes.

删除的内容: very

删除的内容: in

505 The differences between the EN scheme and BR schemes in updraft can be also viewed
506 from the cumulative contoured frequency by altitude diagrams (CCFAD) given in Fig. 8.
507 CCFAD presents the percentage of horizontal grid points with vertical motion weaker than
508 the abscissa scaled value for a given height ([Yuter and Houze, 1995](#)). In this study, vertical
509 speeds are binned with intervals of 1 m s^{-1} based on the even model outputs with six-minute
510 intervals during the severe rainfall episode from 0600 BST to 0700 BST 7 May, 2017.

删除的内容: v

删除的内容: l

删除的内容: ,

511 Generally speaking, the EN scheme shows similar CCFAD patterns to those of the BR scheme.
512 However, there are still differences in the vertical motion. One can see there was a slight
513 weaker core but lower in the EN scheme simulation, compared to those of the BR scheme.

删除的内容: various

514 During the severe rainfall episode, the EN scheme produced the largest updraft nearly 15 m s^{-1}
515 at 5 km level, while that was about 16 m s^{-1} at 6 km level given by the BR scheme. In contrast,
516 updrafts below 6 m s^{-1} occurred more frequently in EN than that in the BR scheme. Overall,
517 the EN scheme provided a larger updraft area but weaker in upward speed, compared to those
518 in BR scheme. This is why the EN scheme had a larger spatial distribution of rainfall than that
519 of the BR scheme (Fig. 6a,b). Note that both EN and BR schemes had a slight difference in

删除的内容: On

带格式的: 字体颜色: 红色

删除的内容: the

删除的内容: slightly

529 downdraft in vertical distribution and the downdraft was mainly located below 2 km, which
530 were also visible in the vertical cross sections (Fig. 7a,b).

531 As has been noted above, both the EN and BR schemes produced very close dynamical
532 patterns except for updrafts. However, differences were remarkable in cloud microphysical
533 processes. Figure 9 compares the temporal evolution of hydrometeors between ~~the EN~~ and
534 BR schemes. One can see that the EN scheme (Fig. 9a-f) produced similar hydrometeors
535 patterns to those of the BR scheme (Fig.9g-i). Overall, graupel was dominant above the
536 melting layer, while rainwater was considerable below the melting layer. Previous studies
537 ([Franklin et al., 2005](#); [Krueger et al., 1995](#); [McCumber et al., 1991](#); [Yin et al., 2018](#)) proposed
538 that graupel was dominant in the tropical and subtropical clouds owing to plentiful water
539 vapor. Overall, the EN scheme mainly increased rainwater content and graupel, while only
540 slight differences in cloud water, cloud ice, snow, and water vapor, compared with those of
541 the BR scheme (Fig. 9m-r).

542 In terms of the difference in rainwater and graupel between the EN and the BR schemes
543 (Fig. 9m-r), we find that the ATC rate of the EN scheme played an important role in the
544 development of deep convection. Compared to the BR scheme, the higher ATC rate of the EN
545 scheme quickly produced more considerable number of small precipitation-sized drops within
546 updrafts in moderate- and lower-levels, and more of the small size raindrops were lofted by
547 the updrafts above the 0 °C level and subsequently were fed for ice processes. Within this
548 graupel coexisted with more small supercooled rainwater region, stronger riming occurred
549 between ice particles and the small size rain drops. Consequently, more of the small
550 supercooled raindrops were converted into graupel by ice cloud microphysical processes such

删除的内容: scheme

552 as riming, leading to a more rapid graupel production. At the same time (Fig. 9q), more
553 supercooled raindrops froze becoming more graupel embryos since bigger raindrops freeze at
554 warmer temperatures than smaller cloud droplets, and continue to grow by riming and/or
555 other processes. Consequently, graupel was increased at high altitude (above the 0 °C) levels.
556 It is well known that bigger water drops freeze at warmer temperatures than small drops.
557 Therefore, partial the small raindrops froze into graupel and snow particles, which contributes
558 to the increment in graupel and snow. Generally, a graupel particle has a larger size than a
559 raindrop with a given mass. Therefore, the larger graupel particle can collect more particles as
560 they fall downward in the storm, which helped create the surface heavy rainfall rate. One can
561 see that the graupel increased rapidly nearly 12 minutes after the appearance of increasing
562 supercooled rain (Fig. 9n). It should be noted we try to understand cloud microphysical
563 processes in the extreme rainfall based on our knowledge at present, and thus a rigorous
564 validation is required by comparing hydrometeors sink and terms in a future study.

565 As the increased graupel passed by the melting level, they started to melt leading to
566 more raindrops. In view of the strong radar reflectivity near the surface in Fig. 7a, the
567 raindrops from upper levels grew rapidly by collecting raindrops in the lower levels. In this
568 way, the extreme rainfall rate was generated in such a more rapid and efficient approach,
569 compared to those of the BR scheme. During this stage, the increased ATC rate was linked to
570 ice-phase processes and modified graupel fraction in the upper levels above the 0 °C. As has
571 been mentioned earlier, the increased ATC rate played a certain role in dynamic feedbacks,
572 and the degree of modulation of water vapor, cloud water, cloud ice, and snow by the
573 increased ATC rate was negligible. These findings indicate that increased ATC rate was

删除的内容: ase

带格式的: 字体颜色: 红色

带格式的: 字体颜色: 红色

带格式的: 字体颜色: 红色

删除的内容: level

带格式的: 字体颜色: 红色

删除的内容: al

删除的内容: were

578 important in the extreme rainfall that involved ice-phase processes of graupel above the 0 °C
579 levels and warm-rain processes of rain drop in the lower levels. To summarize, the higher
580 ATC rate of the EN scheme produced more small precipitation-sized drops, and some of the
581 small size raindrops were lofted the upper levels above the 0 °C. Consequently, more graupel
582 was generated by riming and freezing processes. The rapid production of graupel played a
583 significant role in the development of extreme rainfall. Collision and coalescence processes
584 between liquid particles appeared to be the mechanism of radar reflectivity increment toward
585 the surface within the storm core region.

删除的内容: by

删除的内容: level

删除的内容: were

删除的内容: s

删除的内容: the

586 We proposed the influence mechanism of the ATC rate on the extreme rainfall by
587 comparing the simulated results between the EN scheme and the BR scheme. However, there
588 are still some limitations to figure out the complete effects of the increasing ATC rate on
589 microphysical and dynamical processes at present because those processes are entangled with
590 complicated interactions. Therefore, a better choice is to separate the effects on each process
591 by conducting high-resolution simulations with a sophisticated model, such as the approach of
592 Grabowski (2014). Certainly, the best way is to perform offline testing based on in-situ
593 observations, as was done by Wood (2005). Keeping those issues in our mind, further work is
594 needed to address this question.

595 **6 Conclusions and Discussion**

596 In this study, we designed an ensemble (EN) approach to improving ATC process
597 description in the cloud microphysics schemes. One unique feature of the EN approach is that
598 the ATC rate is a mean value based on the calculations from several widely used ATC schemes.

删除的内容: the

605 Similar to ensemble prediction, this approach is aimed to improve the representation of the
606 ATC rate in case it has been treated by using an ATC scheme alone in the cloud microphysics
607 schemes. At present, the four widely used ATC schemes are selected, including Kessler (1969)
608 scheme, Berry and Reinhardt (1974) scheme, Khairoutdinov and Kogan (2000) scheme, and
609 Liu et al. (2006) scheme. In the EN scheme, each scheme is assigned a weight (Eq. 7) in order
610 to modulate its importance. Certainly, the EN scheme is easily reduced into any single scheme
611 by setting all w_{xx} values of 0 except for one of them. It is also convenient to reduce the effect of
612 a scheme by giving a small value of w_{xx} , even remove the effect of a scheme by assigning a
613 value of weight to 0. Under this framework, the ATC rates from the EN scheme are compared to
614 those from each of the several commonly used schemes by ideal experiments, and a series of
615 simulations are carried out for an urban-induced extreme rainfall event over Southern China
616 by using the EN, KE, BR, KK, and LD schemes which have been coupled into the Thompson
617 scheme in the WRF model (Thompson et al., 2008) in this work. The results show that the EN
618 scheme provides better simulations, compared to those from any single ATC scheme used
619 alone.

删除的内容: the

删除的内容: importanc

删除的内容: e of them

带格式的: 字体颜色: 红色

620 In this study, the ensemble approach has been employed to represent the ATC process in
621 the Thompson cloud microphysics scheme, which shows some advantages for simulation of
622 the extreme rainfall event, occurred on 7 May 2017 over southern China. It is important to
623 acknowledge that the conclusions are drawn from just one case study, and have not been
624 validated under a wider range of conditions over the world. In the forthcoming studies, a
625 systematic assessment of heavier rainfall events is planned to better understand the
626 performance of the EN scheme. It should be noted that there are still some limitations to the

删除的内容: more heavy

带格式的: 字体颜色: 红色

631 EN scheme in the present study. Although a large number of ATC schemes are available, most
632 among them are not employed as ensemble members. For example, the Franklin scheme
633 ([Franklin, 2008](#)) took the effect of turbulence on the ATC process into account, which plays
634 important role in precipitation development ([Chandrakar et al., 2018](#); [Seifert et al., 2010](#)).
635 Furthermore, equal weights were used in the present study for convenience. In other words, the
636 selected schemes have the same effect on the ATC rate. Moreover, only conventional
637 verifications were carried out, and the dependency of the performance of the ATC schemes on
638 the model resolution was not considered in this study. A further examination with new
639 approaches ([e.g., Wood, 2005](#); [Grabowski, 2014](#)) might provide important insights in the near
640 future.

641 ATC is an important process of raindrop initiation in the low-level clouds in general
642 circulation models (GCMS), which has remarkably effects on the models' results (e.g., Golaz
643 et al., 2011; Roy et al., 2021). However, the ATC is sensitive to a ATC scheme, even a
644 parameter, due to heterogeneous cloud properties over the world. Consequently, the EN
645 scheme may be a good option for GCMS in which there are various possible cloud conditions.

带格式的: 字体颜色: 红色

646 It is worth emphasizing that we focus our attention on the ATC from cloud water into rainwater
647 at present. Certainly, any source/sink term in a cloud microphysics scheme can be dealt with
648 with the same method. Since developing a “unified” cloud scheme appears to be a significant
649 part of weather and climate model development in the coming years ([Randall et al., 2019](#)), the
650 EN approach may be a practicable way to reduce the potential uncertainty in cloud and
651 precipitation physical process, which will contribute to more accurate numerical model
652 development.

653

654 **Code and data availability:** The source code of the Weather Research and Forecasting model
 655 (WRF v4.1.3) is available at <https://github.com/wrf-model/WRF/releases> (last access: July
 656 2021). Modified WRF model codes and initial and boundary data used for the simulations are
 657 available on Zenodo (<https://doi.org/10.5281/zenodo.5052639>). The National Centers for
 658 Environmental Prediction (NCEP) Global Forecast System 0.25 degree final-analysis data at
 659 6-h intervals used for the initial and boundary conditions for the specific analysed period can
 660 be downloaded at <https://rda.ucar.edu/datasets/ds083.2/>.

删除的内容: re

661 **Competing interests:** The author declares no competing interests.

662 **Author contributions.** J. Yin developed the weighted ensemble scheme and coupled the
 663 scheme into the WRF model, with contributions from X. Liang. J. Yin tested and verified the
 664 scheme with contributions from X. Liang, H. Wang, and H Xue. J. Yin wrote the manuscript,
 665 and all the authors continuously discussed the results and contributed to the improvement of
 666 the paper text.

667 **Acknowledgements:** This study is jointly supported by the National Natural Science
 668 Foundation of China (42075083), and National Key Research and Development Program of
 669 China (2018YFC1507404 and 2017YFC1501806). The authors also acknowledge the use of
 670 the NCAR Command Language (NCL) in the analysis of some of the WRF Model output and
 671 the preparation of figures. The authors are thankful to the Chief editor (Astrid Kerkweg), the
 672 handling topical deitor (David Topping), and two anonymous reviewers for their help
 673 improving the manuscript,

带格式的: 字体: (中文) Times New Roman

删除的内容: ,

带格式的: 字体: (默认) Times New Roman, (中文) Times New Roman

带格式的: 字体: (默认) Times New Roman, (中文) Times New Roman

删除的内容: , and Development Foundation of Chinese Academy of Meteorological Sciences (2019KJ026)

带格式的

674

680 **References:**

- 681 Bao, X., Wu, L., Tang, B., Ma, L., Wu, D., Tang, J., Chen, H., and Wu, L.: Variable
682 Raindrop Size Distributions in Different Rainbands Associated With Typhoon
683 Fitow (2013), *J. Geophys. Res.: Atmos.*, 124, 12262-12281,
684 <https://doi.org/10.1029/2019JD030268>, 2019.
- 685 Bao, X., Wu, L., Zhang, S., Li, Q., Lin, L., Zhao, B., Wu, D., Xia, W., and Xu, B.:
686 Distinct Raindrop Size Distributions of Convective Inner- and Outer-Rainband
687 Rain in Typhoon Maria (2018), *J. Geophys. Res.: Atmos.*, 125, e2020JD032482,
688 <https://doi.org/10.1029/2020JD032482>, 2020.
- 689 Beheng, K. D.: A parameterization of warm cloud microphysical conversion processes,
690 *Atmos. Res.*, 33, 193-206, [https://doi.org/10.1016/0169-8095\(94\)90020-5](https://doi.org/10.1016/0169-8095(94)90020-5) , 1994.
- 691 Berry, E. X.: Modification o the warm rain process. Preprints, First National Conf. on
692 Weather Modification, Albany, NY, Amer. Meteor. Soc., 81–88, 1968.
- 693 Berry, E. X. and Reinhardt, R. L.: An Analysis of Cloud Drop Growth by Collection
694 Part II. Single Initial Distributions, *J. Atmos. Sci.*, 31, 1825-1831,
695 [https://doi.org/10.1175/1520-0469\(1974\)031<1825:aaocdg>2.0.co;2](https://doi.org/10.1175/1520-0469(1974)031<1825:aaocdg>2.0.co;2), 1974.
- 696 Caro, D., Wobrock, W., Flossmann, A. I., and Chaumerliac, N.: A two-moment
697 parameterization of aerosol nucleation and impaction scavenging for a warm
698 cloud microphysics: description and results from a two-dimensional simulation,
699 *Atmos. Res.*, 70, 171-208, <http://dx.doi.org/10.1016/j.atmosres.2004.01.002>,
700 2004.
- 701 Chandrakar, K. K., Cantrell, W., and Shaw, R. A.: Influence of Turbulent Fluctuations
702 on Cloud Droplet Size Dispersion and Aerosol Indirect Effects, *J. Atmos. Sci.*, 75,
703 3191-3209, <https://doi.org/10.1175/JAS-D-18-0006.1>, 2018.
- 704 Chen, S.-H. and Sun, W.-Y.: A One-dimensional Time Dependent Cloud Model, *J.*
705 *Meteor. Soc. Japan*, 80, 99-118, <https://doi.org/10.2151/jmsj.80.99>, 2002.
- 706 Cotton, W. R.: Numerical Simulation of Precipitation Development in Supercooled
707 Cumuli—Part I, *Mon. Wea. Rev.*, 100, 757-763,
708 [https://doi.org/10.1175/1520-0493\(1972\)100<0757:NSOPDI>2.3.CO;2](https://doi.org/10.1175/1520-0493(1972)100<0757:NSOPDI>2.3.CO;2), 1972.
- 709 Doswell, C. A., III: Severe Convective Storms—An Overview, *Meteor. Monogr.*, 50,
710 1-26, <https://doi.org/10.1175/0065-9401-28.50.1>, 2001.
- 711 | [Dudhia, J.: Numerical Study of Convection Observed during the Winter Monsoon](#)
712 Experiment Using a Mesoscale Two-Dimensional Model, *J. Atmos. Sci.*, 46,

删除的内容: Duan, Y., Wan, Q., Huang, J., Zhao, K., Yu, H., Wang, Y., Zhao, D., Feng, J., Tang, J., Chen, P., Lu, X., Wang, Y., Liang, J., Wu, L., Cui, X., Xu, J., and Chan, P.-W.: Landfalling Tropical Cyclone Research Project (LTCRP) in China, *Bull. Amer. Meteor. Soc.*, 100, ES447-ES472, <https://doi.org/10.1175/BAMS-D-18-0241.1>, 2020. .

724 3077-3107,
725 [https://doi.org/10.1175/1520-0469\(1989\)046<3077:NSOCOD>2.0.CO;2](https://doi.org/10.1175/1520-0469(1989)046<3077:NSOCOD>2.0.CO;2), 1989.
726 Falk, N. M., Igel, A. L., and Igel, M. R.: The relative impact of ice fall speeds and
727 microphysics parameterization complexity on supercell evolution, *Mon. Wea.*
728 *Rev.*, 147, 2403-2415, <https://doi.org/10.1175/MWR-D-18-0417.1>, 2019.
729 FlatøY, F.: Comparison of two parameterization schemes for cloud and precipitation
730 processes, *Tellus A: Dyn. Meteor. Ocean.*, 44, 41-53,
731 <https://doi.org/10.3402/tellusa.v44i1.14942>, 1992.
732 Franklin, C. N.: A Warm Rain Microphysics Parameterization that Includes the Effect
733 of Turbulence, *J. Atmos. Sci.*, 65, 1795-1816,
734 <https://doi.org/10.1175/2007JAS2556.1>, 2008.
735 Franklin, C. N., Holland, G. J., and May, P. T.: Sensitivity of Tropical Cyclone
736 Rainbands to Ice-Phase Microphysics, *Mon. Wea. Rev.*, 133, 2473-2493,
737 <https://doi.org/10.1175/MWR2989.1>, 2005.
738 Freeman, S. W., Igel, A. L., and van den Heever, S. C.: Relative sensitivities of
739 simulated rainfall to fixed shape parameters and collection efficiencies, *Quart. J.*
740 *Royal Meteor. Soc.*, 145, 2181-2201, <https://doi.org/10.1002/qj.3550>, 2019.
741 Fu, H. and Lin, Y.: A Kinematic Model for Understanding Rain Formation Efficiency
742 of a Convective Cell, *J. Adv. Model. Earth Sy.*, 11, 4395-4422,
743 <https://doi.org/10.1029/2019MS001707>, 2019.
744 Ghosh, S. and Jonas, P. R.: On the application of the classic Kessler and Berry schemes
745 in Large Eddy Simulation models with a particular emphasis on cloud
746 autoconversion, the onset time of precipitation and droplet evaporation, *Ann.*
747 *Geophys.*, 16, 628-637, <https://doi.org/10.1007/s00585-998-0628-2>, 1999.
748 Gilmore, M. S. and Straka, J. M.: The Berry and Reinhardt Autoconversion
749 Parameterization: A Digest, *J. Appl. Meteor. Clim.*, 47, 375-396,
750 <https://doi.org/10.1175/2007JAMC1573.1>, 2008.
751 Gilmore, M. S., Straka, J. M., and Rasmussen, E. N.: Precipitation uncertainty due to
752 variations in precipitation particle parameters within a simple microphysics
753 scheme, *Mon. Wea. Rev.*, 132, 2610-2627, <https://doi.org/10.1175/MWR2810.1>,
754 2004.
755 Grabowski, W. W., Wu, X., and Moncrieff, M. W.: Cloud Resolving Modeling of
756 Tropical Cloud Systems during Phase III of GATE. Part III: Effects of Cloud
757 Microphysics, *J. Atmos. Sci.*, 56, 2384-2402,

758 [https://doi.org/10.1175/1520-0469\(1999\)056<2384:CRMOTC>2.0.CO;2](https://doi.org/10.1175/1520-0469(1999)056<2384:CRMOTC>2.0.CO;2), 1999.

759 Grabowski, W. W.: Extracting Microphysical Impacts in Large-Eddy Simulations of
760 Shallow Convection, *J. Atmos. Sci.*, 71, 4493-4499,
761 <https://doi.org/10.1175/JAS-D-14-0231.1>, 2014.

762 Grabowski, W. W., Morrison, H., Shima, S.-I., Abade, G. C., Dziekan, P., and
763 Pawlowska, H.: Modeling of Cloud Microphysics: Can We Do Better?, *Bull.*
764 *Amer. Meteor. Soc.*, 100, 655-672, <https://doi.org/10.1175/BAMS-D-18-0005.1>,
765 2019.

766 Griffin, B. M. and Larson, V. E.: Analytic upscaling of a local microphysics scheme.
767 Part II: Simulations, *Quart. J. Royal Meteor. Soc.*, 139, 58-69,
768 <https://doi.org/10.1002/qj.1966>, 2013.

769 Hong, S.-Y., Noh, Y., and Dudhia, J.: A new vertical diffusion package with an explicit
770 treatment of entrainment processes, *Mon. Wea. Rev.*, 134, 2318-2341,
771 <https://doi.org/10.1175/MWR3199.1>, 2006.

772 Houghton, J. T., Ding, Y. H., Griggs, D. J., Noguer, M., Linden, P. J. v. d., Dai, X.,
773 K.Maskell, and Johnson, C. A. (Eds.): *Climate Change 2001: The Scientific Basis*,
774 Cambridge University Press, Cambridge, 49 pp., 2001.

775 Hsieh, W. C., Jonsson, H., Wang, L. P., Buzorius, G., Flagan, R. C., Seinfeld, J. H., and
776 Nenes, A.: On the representation of droplet coalescence and autoconversion:
777 Evaluation using ambient cloud droplet size distributions, *J. Geophys. Res.:*
778 *Atmos.*, 114, <https://doi.org/10.1029/2008JD010502>, 2009.

779 Iacobellis, S. F. and Somerville, R. C. J.: Evaluating parameterizations of the
780 autoconversion process using a single-column model and Atmospheric Radiation
781 Measurement Program measurements, *J. Geophys. Res.: Atmos.*, 111, n/a-n/a,
782 <https://doi.org/10.1029/2005jd006296>, 2006.

783 Janjić, Z. I.: The step-mountain eta coordinate model: further developments of the
784 convection, viscous sublayer, and turbulence closure schemes, *Mon. Wea. Rev.*,
785 122, 927-945,
786 [https://doi.org/10.1175/1520-0493\(1994\)122<0927:TSMECM>2.0.CO;2](https://doi.org/10.1175/1520-0493(1994)122<0927:TSMECM>2.0.CO;2), 1994.

787 Jing, X., Suzuki, K., and Michibata, T.: The Key Role of Warm Rain Parameterization
788 in Determining the Aerosol Indirect Effect in a Global Climate Model, *J. Climate*,
789 32, 4409-4430, <https://doi.org/10.1175/JCLI-D-18-0789.1>, 2019.

790 Kain, J. S.: The Kain–Fritsch Convective Parameterization: An Update, *J. Appl.*
791 *Meteor.*, 43, 170-181,

792 [https://doi.org/10.1175/1520-0450\(2004\)043<0170:TKCPAU>2.0.CO;2](https://doi.org/10.1175/1520-0450(2004)043<0170:TKCPAU>2.0.CO;2), 2004.

793 Kessler, E.: On the Distribution and Continuity of Water Substance in Atmospheric
794 Circulations, *Circulations. Meteor. Monogr.*, 10. American Meteorological
795 Society, Boston 1969.

796 Khain, A. P., Beheng, K. D., Heymsfield, A., Korolev, A., Krichak, S. O., Levin, Z.,
797 Pinsky, M., Phillips, V., Prabhakaran, T., Teller, A., van den Heever, S. C., and
798 Yano, J. I.: Representation of microphysical processes in cloud-resolving models:
799 Spectral (bin) microphysics versus bulk parameterization, *Rev. Geophys.*, 53,
800 2014RG000468, <https://doi.org/10.1002/2014RG000468>, 2015.

801 Khairoutdinov, M. and Kogan, Y.: A New Cloud Physics Parameterization in a
802 Large-Eddy Simulation Model of Marine Stratocumulus, *Mon. Wea. Rev.*, 128,
803 229-243, [https://doi.org/10.1175/1520-0493\(2000\)128<0229:ancppi>2.0.co;2](https://doi.org/10.1175/1520-0493(2000)128<0229:ancppi>2.0.co;2),
804 2000.

805 Kogan, Y. and Ovchinnikov, M.: Formulation of Autoconversion and Drop Spectra
806 Shape in Shallow Cumulus Clouds, *J. Atmos. Sci.*, 77, 711-722,
807 <https://doi.org/10.1175/JAS-D-19-0134.1>, 2019.

808 Kong, F. and Yau, M. K.: An explicit approach to microphysics in MC2, *Atmos.-Ocean*,
809 35, 257-291, <https://doi.org/10.1080/07055900.1997.9649594>, 1997.

810 Krueger, S. K., Fu, Q., Liou, K. N., and Chin, H.-N. S.: Improvements of an Ice-Phase
811 Microphysics Parameterization for Use in Numerical Simulations of Tropical
812 Convection, *J. Appl. Meteor.*, 34, 281-287,
813 <https://doi.org/10.1175/1520-0450-34.1.281>, 1995.

814 Lee, H. and Baik, J.-J.: A physically based autoconversion parameterization, *J. Atmos.*
815 *Sci.*, 74, 1599-1616, <https://doi.org/10.1175/JAS-D-16-0207.1>, 2017.

816 Lei, H., Guo, J., Chen, D., and Yang, J.: Systematic Bias in the Prediction of
817 Warm-Rain Hydrometeors in the WDM6 Microphysics Scheme and
818 Modifications, *J. Geophys. Res.: Atmos.*, 125, e2019JD030756,
819 <https://doi.org/10.1029/2019JD030756>, 2020.

820 Lewis, J. M.: Roots of Ensemble Forecasting, *Mon. Wea. Rev.*, 133, 1865-1885,
821 <https://doi.org/10.1175/MWR2949.1>, 2005.

822 Li, M., Luo, Y., Zhang, D.-L., Chen, M., Wu, C., Yin, J., and Ma, R.: Analysis of a
823 record-breaking rainfall event associated with a monsoon coastal megacity of
824 south China using multi-source data, *IEEE Trans. Geosci. Remote Sens.*,
825 <https://doi.org/10.1109/TGRS.2020.3029831>, 2020.

826 Li, X.-Y., Brandenburg, A., Svensson, G., Haugen, N. E. L., Mehlh, B., and
827 Rogachevskii, I.: Condensational and Collisional Growth of Cloud Droplets in a
828 Turbulent Environment, *J. Atmos. Sci.*, 77, 337-353,
829 <https://doi.org/10.1175/JAS-D-19-0107.1>, 2019.

830 Lin, B., Zhang, J., and Lohmann, U.: A New Statistically based Autoconversion rate
831 Parameterization for use in Large-Scale Models, *J. Geophys. Res. : Atmos.*, 107,
832 <https://doi.org/10.1029/2001JD001484>, 2002.

833 Liu, Y. and Daum, P. H.: Parameterization of the Autoconversion Process.Part I:
834 Analytical Formulation of the Kessler-Type Parameterizations, *J. Atmos. Sci.*, 61,
835 1539-1548,
836 [https://doi.org/10.1175/1520-0469\(2004\)061<1539:POTAPI>2.0.CO;2](https://doi.org/10.1175/1520-0469(2004)061<1539:POTAPI>2.0.CO;2), 2004.

837 Liu, Y., Daum, P. H., McGraw, R., and Wood, R.: Parameterization of the
838 Autoconversion Process. Part II: Generalization of Sundqvist-Type
839 Parameterizations, *J. Atmos. Sci.*, 63, 1103-1109,
840 <https://doi.org/10.1175/jas3675.1>, 2006.

841 Manton, M. J. and Cotton, W. R.: Parameterization of the Atmospheric Surface Layer, *J.*
842 *Atmos. Sci.*, 34, 331-334,
843 [https://doi.org/10.1175/1520-0469\(1977\)034<0331:POTASL>2.0.CO;2](https://doi.org/10.1175/1520-0469(1977)034<0331:POTASL>2.0.CO;2), 1977a.

844 Manton, M. I. and Cotton, W. R.: Formulation of Approximate Equations for Modeling
845 Moist Deep Convection on the Mesoscale. Atmospheric Science Paper 266,
846 Colorado State University, 62 pp, 1977b.

847 McCumber, M., Tao, W.-K., Simpson, J., Penc, R., and Soong, S.-T.: Comparison of
848 Ice-Phase Microphysical Parameterization Schemes Using Numerical Simulations
849 of Tropical Convection, *J. Appl. Meteor.*, 30, 985-1004,
850 <https://doi.org/10.1175/1520-0450-30.7.985>, 1991.

851 Michibata, T. and Takemura, T.: Evaluation of autoconversion schemes in a single
852 model framework with satellite observations, *J. Geophys. Res.: Atmos.*, 120,
853 9570-9590, <https://doi.org/10.1002/2015JD023818>, 2015.

854 Mlawer, E. J., Taubman, S. J., Brown, P. D., Iacono, M. J., and Clough, S. A.: Radiative
855 transfer for inhomogeneous atmospheres: RRTM, a validated correlated-k model
856 for the longwave, *J. Geophys. Res.: Atmos.*, 102, 16663-16682,
857 <https://doi.org/10.1029/97JD00237>, 1997.

858 Morrison, H., Thompson, G., and Tatarskii, V.: Impact of Cloud Microphysics on the
859 Development of Trailing Stratiform Precipitation in a Simulated Squall Line :

860 Comparison of One-and Two-Moment Schemes, *Mon. Wea. Rev.*, 137, 991-1007,
 861 <https://doi.org/10.1175/2008MWR2556.1>, 2009.

862 Morrison, H., van Lier-Walqui, M., Fridlind, A. M., Grabowski, W. W., Harrington, J.
 863 Y., Hoose, C., Korolev, A., Kumjian, M. R., Milbrandt, J. A., Pawlowska, H.,
 864 Posselt, D. J., Prat, O. P., Reimel, K. J., Shima, S.-I., van Dierenhoven, B., and
 865 Xue, L.: Confronting the Challenge of Modeling Cloud and Precipitation
 866 Microphysics, *J. Adv. Model. Earth Sy.*, 12, e2019MS001689,
 867 <https://doi.org/10.1029/2019MS001689>, 2020.

868 Naeger, A. R., Colle, B. A., Zhou, N., and Molthan, A.: Evaluating Warm and Cold
 869 Rain Processes in Cloud Microphysical Schemes Using OLYMPEX Field
 870 Measurements, *Mon. Wea. Rev.*, 148, 2163-2190,
 871 <https://doi.org/10.1175/MWR-D-19-0092.1>, 2020.

872 Niu, G.-Y., Yang, Z.-L., Mitchell, K. E., Chen, F., Ek, M. B., Barlage, M., Kumar, A.,
 873 Manning, K., Niyogi, D., Rosero, E., Tewari, M., and Xia, Y.: The community
 874 Noah land surface model with multiparameterization options (Noah-MP): 1.
 875 Model description and evaluation with local-scale measurements, *J. Geophys.*
 876 *Res.: Atmos.*, 116, D12109, <https://doi.org/10.1029/2010JD015139>, 2011.

877 Onishi, R., Matsuda, K., and Takahashi, K.: Lagrangian Tracking Simulation of Droplet
 878 Growth in Turbulence–Turbulence Enhancement of Autoconversion Rate*, *J.*
 879 *Atmos. Sci.*, 72, 2591-2607, <https://doi.org/10.1175/JAS-D-14-0292.1>, 2015.

880 Pawlowska, H., and Brenguier, J. L.: A study of the microphysical structure of
 881 stratocumulus clouds. Proc. 12th Int. Conf. Clouds and precipitation, Zurich, Ed.
 882 P. R. Jones, Published by Page Bros., Norwich, U.K., 123-126, 1996.

883 Posselt, D. J., He, F., Bukowski, J., and Reid, J. S.: On the Relative Sensitivity of a
 884 Tropical Deep Convective Storm to Changes in Environment and Cloud
 885 Microphysical Parameters, *J. Atmos. Sci.*, 76, 1163-1185,
 886 <https://doi.org/10.1175/JAS-D-18-0181.1>, 2019.

887 Randall, D. A., Bitz, C. M., Danabasoglu, G., Denning, A. S., Gent, P. R., Gettelman,
 888 A., Griffies, S. M., Lynch, P., Morrison, H., Pincus, R., and Thuburn, J.: 100 Years
 889 of Earth System Model Development, *Meteor. Monogr.*, 59, 12.11-12.66,
 890 <https://doi.org/10.1175/AMSMONOGRAPHS-D-18-0018.1>, 2019.

891 Reen, B.: A brief guide to observation nudging in WRF,
 892 <https://www2.mmm.ucar.edu/wrf/users/docs/ObsNudgingGuide.pdf>, 2016.

893 Reisner, J., Rasmussen, R. M., and Bruintjes, R. T.: Explicit forecasting of supercooled

带格式的: 字体: 小四

带格式的: 缩进: 左侧: 0 厘米,
悬挂缩进: 2 字符

带格式的: 字体: 小四

删除的内容: .

带格式的: 字体: (中文) +中文正
文 (宋体)

895 liquid water in winter storms using the MM5 mesoscale model, *Quart. J. Roy.*
896 *Meteor. Soc.*, 124, 1071-1107, <https://doi.org/10.1002/qj.49712454804> 1998.

897 Rutledge, S. A. and Hobbs, P. V.: The Mesoscale and Microscale Structure and
898 Organization of Clouds and Precipitation in Midlatitude Cyclones. XII: A
899 Diagnostic Modeling Study of Precipitation Development in Narrow Cold-Frontal
900 Rainbands, *J. Atmos. Sci.*, 41, 2949-2972,
901 [https://doi.org/10.1175/1520-0469\(1984\)041<2949:TMAMSA>2.0.CO;2](https://doi.org/10.1175/1520-0469(1984)041<2949:TMAMSA>2.0.CO;2), 1984.

902 Schultz, P.: An Explicit Cloud Physics Parameterization for Operational Numerical
903 Weather Prediction, *Mon. Wea. Rev.*, 123, 3331-3343,
904 [https://doi.org/10.1175/1520-0493\(1995\)123<3331:AECPPF>2.0.CO;2](https://doi.org/10.1175/1520-0493(1995)123<3331:AECPPF>2.0.CO;2), 1995.

905 Seifert, A. and Beheng, K. D.: A double-moment parameterization for simulating
906 autoconversion, accretion and selfcollection, *Atmos. Res.*, 59-60, 265-281,
907 [https://doi.org/10.1016/S0169-8095\(01\)00126-0](https://doi.org/10.1016/S0169-8095(01)00126-0), 2001.

908 Seifert, A., Nuijens, L., and Stevens, B.: Turbulence effects on warm-rain
909 autoconversion in precipitating shallow convection, *Quart. J. Royal Meteor. Soc.*,
910 136, 1753-1762, <https://doi.org/10.1002/qj.684>, 2010.

911 Silverman, B. A. and Glass, M.: A Numerical Simulation of Warm Cumulus Clouds:
912 Part I. Parameterized vs Non-Parameterized Microphysics, *J. Atmos. Sci.*, 30,
913 1620-1637,
914 [https://doi.org/10.1175/1520-0469\(1973\)030<1620:ANSOWC>2.0.CO;2](https://doi.org/10.1175/1520-0469(1973)030<1620:ANSOWC>2.0.CO;2), 1973.

915 Simpson, j. and Wiggert, v.: Models of precipitating cumulus towers, *Mon. Wea. Rev.*,
916 97, 471-489,
917 [https://doi.org/10.1175/1520-0493\(1969\)097<0471:MOPCT>2.3.CO;2](https://doi.org/10.1175/1520-0493(1969)097<0471:MOPCT>2.3.CO;2), 1969.

918 Skamarock, W. C., Klemp, J. B., Duda, M. G., Fowler, L. D., Park, S.-H., and Ringler, T.
919 D.: A Multiscale Nonhydrostatic Atmospheric Model Using Centroidal Voronoi
920 Tessellations and C-Grid Staggering, *Mon. Wea. Rev.*, 140, 3090-3105,
921 <https://doi.org/10.1175/MWR-D-11-00215.1>, 2012.

922 Skamarock, W. C., Klemp, J. B., Dudhia, J., Gill, D. O., Liu, Z., Berner, J., Wang, W.,
923 Powers, J. G., Duda, M. G., Barker, D. M., and Huang, X.-Y.: A Description of the
924 Advanced Research WRF Version 4. NCAR Tech. Note NCAR/TN-556+STR,
925 145 pp, <https://doi.org/10.5065/1dfh-6p97>, 2019.

926 Sundqvist, H., Berge, E., and Kristjánsson, J. E.: Condensation and Cloud
927 Parameterization Studies with a Mesoscale Numerical Weather Prediction Model,
928 *Mon. Wea. Rev.*, 117, 1641-1657,

929 [https://doi.org/10.1175/1520-0493\(1989\)117<1641:cacpsw>2.0.co;2](https://doi.org/10.1175/1520-0493(1989)117<1641:cacpsw>2.0.co;2), 1989.

930 Tao, W.-K. and Simpson, J.: Goddard Cumulus Ensemble Model. Part I: Model
 931 Description, *Terr. Atmos. Oceanic Sci.*, 4, 35-72,
 932 [https://doi.org/10.3319/TAO.1993.4.1.35\(A\)](https://doi.org/10.3319/TAO.1993.4.1.35(A)), 1993.

933 Tapiador, F. J., Sánchez, J.-L., and García-Ortega, E.: Empirical values and
 934 assumptions in the microphysics of numerical models, *Atmos. Res.*, 215, 214-238,
 935 <https://doi.org/10.1016/j.atmosres.2018.09.010>, 2019.

936 Thompson, G., Rasmussen, R. M., and Manning, K.: Explicit Forecasts of Winter
 937 Precipitation Using an Improved Bulk Microphysics Scheme. Part I: Description
 938 and Sensitivity Analysis, *Mon. Wea. Rev.*, 132, 519-542,
 939 [https://doi.org/10.1175/1520-0493\(2004\)132<0519:EFOWPU>2.0.CO;2](https://doi.org/10.1175/1520-0493(2004)132<0519:EFOWPU>2.0.CO;2), 2004.

940 Thompson, G., Field, P. R., Rasmussen, R. M., and Hall, W. D.: Explicit Forecasts of
 941 Winter Precipitation Using an Improved Bulk Microphysics Scheme. Part II:
 942 Implementation of a New Snow Parameterization, *Mon. Wea. Rev.*, 136,
 943 5095-5115, <https://doi.org/10.1175/2008MWR2387.1>, 2008.

944 Wellmann, C., Barrett, A. I., Johnson, J. S., Kunz, M., Vogel, B., Carslaw, K. S., and
 945 Hoose, C.: Comparing the impact of environmental conditions and microphysics
 946 on the forecast uncertainty of deep convective clouds and hail, *Atmos. Chem.
 947 Phys.*, 20, 2201-2219, <https://doi.org/10.5194/acp-20-2201-2020>, 2020.

948 White, B., Gryspeerdt, E., Stier, P., Morrison, H., Thompson, G., and Kipling, Z.:
 949 Uncertainty from the choice of microphysics scheme in convection-permitting
 950 models significantly exceeds aerosol effects, *Atmos. Chem. Phys.*, 17,
 951 12145-12175, <https://doi.org/10.5194/acp-17-12145-2017>, 2017.

952 Wood, R.: Drizzle in Stratiform Boundary Layer Clouds. Part II: Microphysical
 953 Aspects, *J. Atmos. Sci.*, 62, 3034-3050, <https://doi.org/10.1175/JAS3530.1>, 2005.

954 Wood, R. and Blossey, P. N.: Comments on “Parameterization of the Autoconversion
 955 Process. Part I: Analytical Formulation of the Kessler-Type Parameterizations”, *J.
 956 Atmos. Sci.*, 62, 3003-3006, <https://doi.org/10.1175/jas3524.1>, 2005.

957 Wood, R., Field, P. R., and Cotton, W. R.: Autoconversion rate bias in stratiform
 958 boundary layer cloud parameterizations, *Atmos. Res.*, 65, 109-128,
 959 [http://dx.doi.org/10.1016/S0169-8095\(02\)00071-6](http://dx.doi.org/10.1016/S0169-8095(02)00071-6), 2002.

960 Xiao, H., Yin, Y., Zhao, P., Wan, Q., and Liu, X.: Effect of Aerosol Particles on
 961 Orographic Clouds: Sensitivity to Autoconversion Schemes, *Advances in
 962 Atmospheric Sciences*, 37, 229-238, <https://doi.org/10.1007/s00376-019-9037-6>,

963 2020.

964 Yin, J.-F., Wang, D.-H., Liang, Z.-M., Liu, C.-J., Zhai, G.-Q., and Wang, H.: Numerical
965 Study of the Role of Microphysical Latent Heating and Surface Heat Fluxes in a
966 Severe Precipitation Event in the Warm Sector over Southern China, *Asia-Pacific*
967 *J. Atmos. Sci.*, 54, 77-90, <https://doi.org/10.1007/s13143-017-0061-0>, 2018.

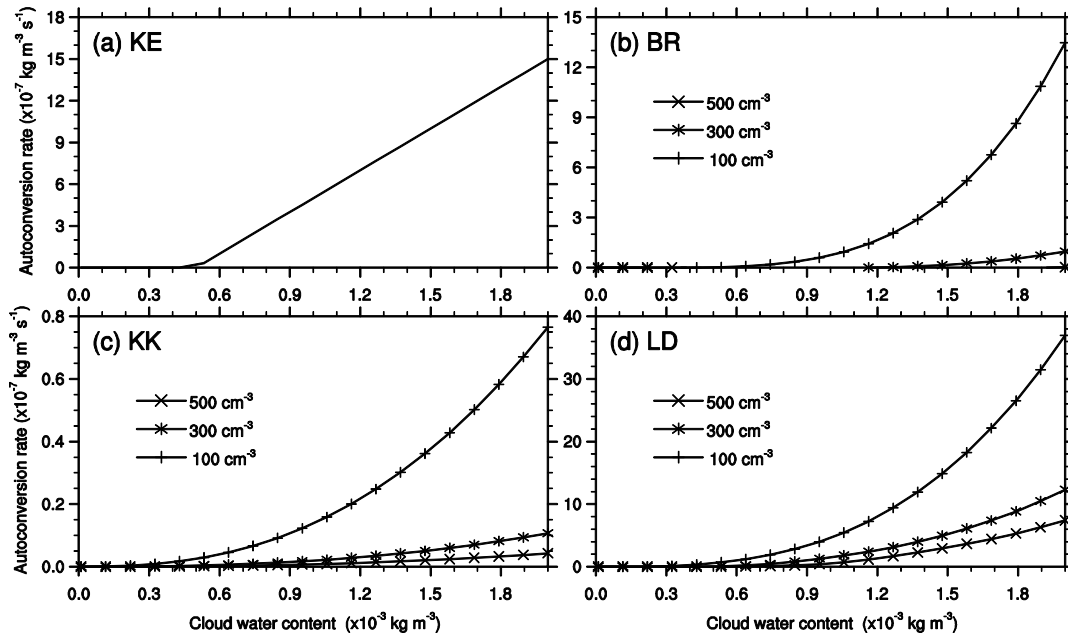
968 Yin, J., Wang, D., and Zhai, G.: An attempt to improve Kessler-type parameterization
969 of warm cloud microphysical conversion processes using CloudSat observations, *J.*
970 *Meteorol. Res.*, 29, 82-92, <https://doi.org/10.1007/s13351-015-4091-1>, 2015.

971 Yin, J., Zhang, D.-L., Luo, Y., and Ma, R.: On the Extreme Rainfall Event of 7 May
972 2017 Over the Coastal City of Guangzhou. Part I: Impacts of Urbanization and
973 Orography, *Mon. Wea. Rev.*, <https://doi.org/10.1175/MWR-D-19-0212.1>, 2020.

974 Yuter, S. E. and Houze, R. A.: Three-Dimensional Kinematic and Microphysical
975 Evolution of Florida Cumulonimbus. Part II: Frequency Distributions of Vertical
976 Velocity, Reflectivity, and Differential Reflectivity, *Mon. Wea. Rev.*, 123,
977 1941-1963,
978 [https://doi.org/10.1175/1520-0493\(1995\)123<1941:TDKAME>2.0.CO;2](https://doi.org/10.1175/1520-0493(1995)123<1941:TDKAME>2.0.CO;2), 1995.

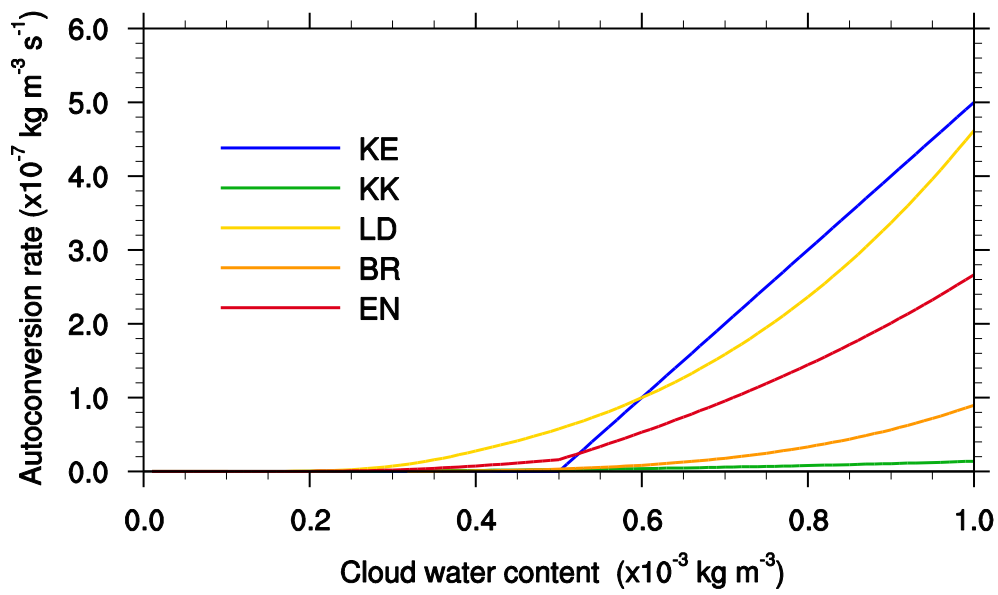
979 Zhang, Y., Li, J., Yu, R., Zhang, S., Liu, Z., Huang, J., and Zhou, Y.: A Layer-Averaged
980 Nonhydrostatic Dynamical Framework on an Unstructured Mesh for Global and
981 Regional Atmospheric Modeling: Model Description, Baseline Evaluation, and
982 Sensitivity Exploration, *J. Adv. Model. Earth Sy.*, 11, 1685-1714,
983 <https://doi.org/10.1029/2018MS001539>, 2019

Figures



868

869 **Fig. 1** Evolution of autoconversion rates with a wide range of cloud water
 870 content at given cloud number concentrations (N_c) of 100 cm^{-3} , 300 cm^{-3} , and 500
 871 cm^{-3} , respectively. (a) KE denotes the Kessler scheme ([1969](#)), and (b) BR indicates
 872 the Berry and Reinhardt scheme ([1974](#)); (c) KK and (d) LD represents the
 873 Khairoutdinov and Kogan ([2000](#)) and Liu et al. (LD) schemes ([2006](#)), respectively.



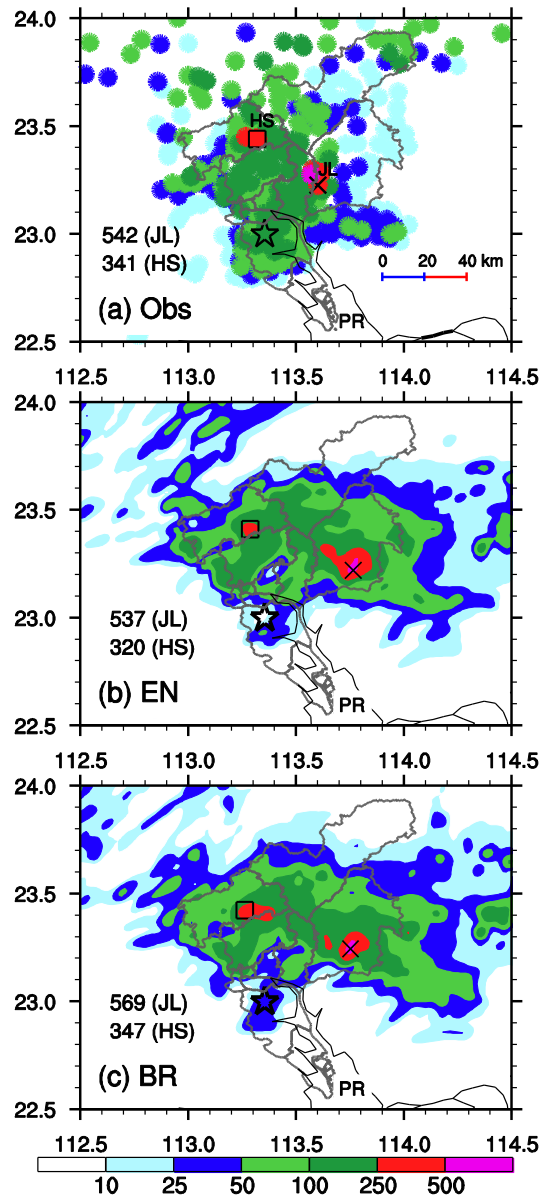
874

875

Fig. 2 Comparisons of the EN scheme with the selected KE, BR, KK, and LD

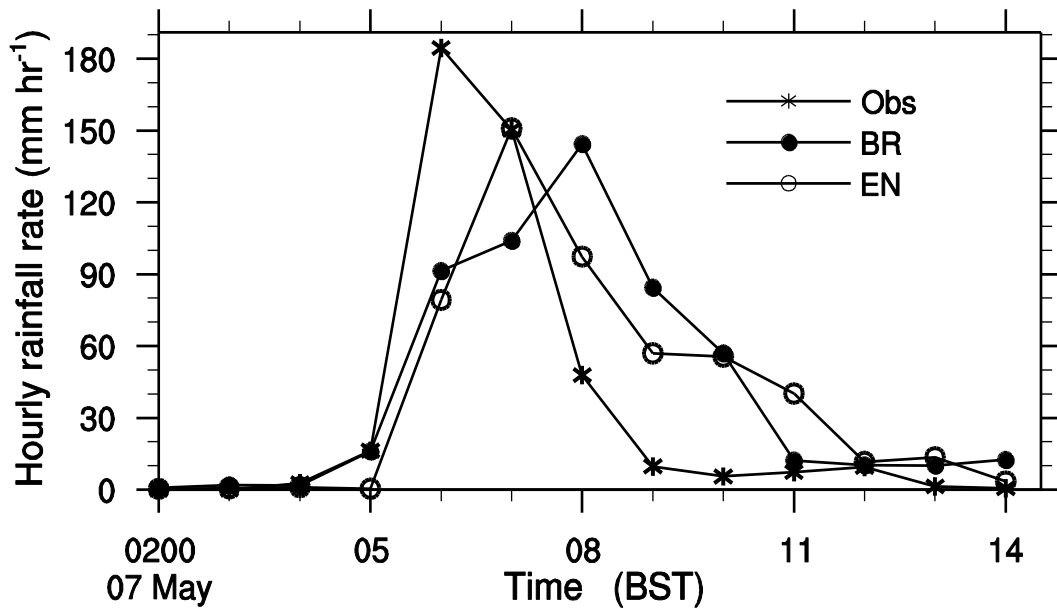
876

schemes at a fixed N_c of 300 cm^{-3} . (see text for further details)



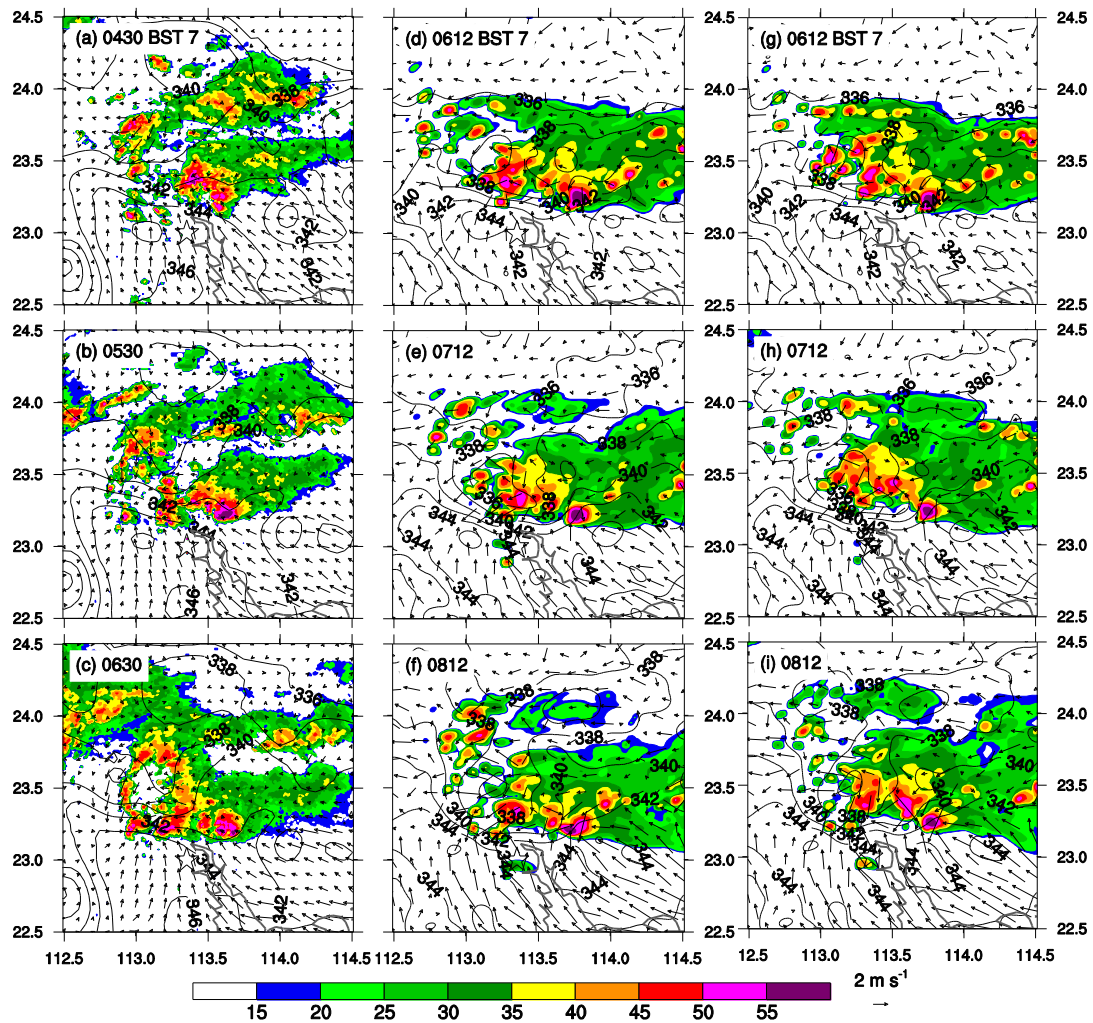
877

878 **Fig. 3** Spatial distribution of the 18-h accumulated rainfall during the period of
 879 2000 BST 6 May to 1400 BST 7 May, 2017: (a) rain gauge observations and (b-c)
 880 simulations with the EN and BR autoconversion schemes. A cross sign (×) and a
 881 square sign (□) denote the locations where maximum hourly rainfall rates were (a)
 882 observed or (b-c) simulated near Jiulong (JL) and Huashan(HS), respectively. The
 883 values marked with JL and HS indicate the 18-h maximum accumulated rainfall
 884 amounts near the JL and HS, respectively. A star indicates the city center of Guangzhou,
 885 and the Pearl River is marked by PR; similarly for the rest of figures.



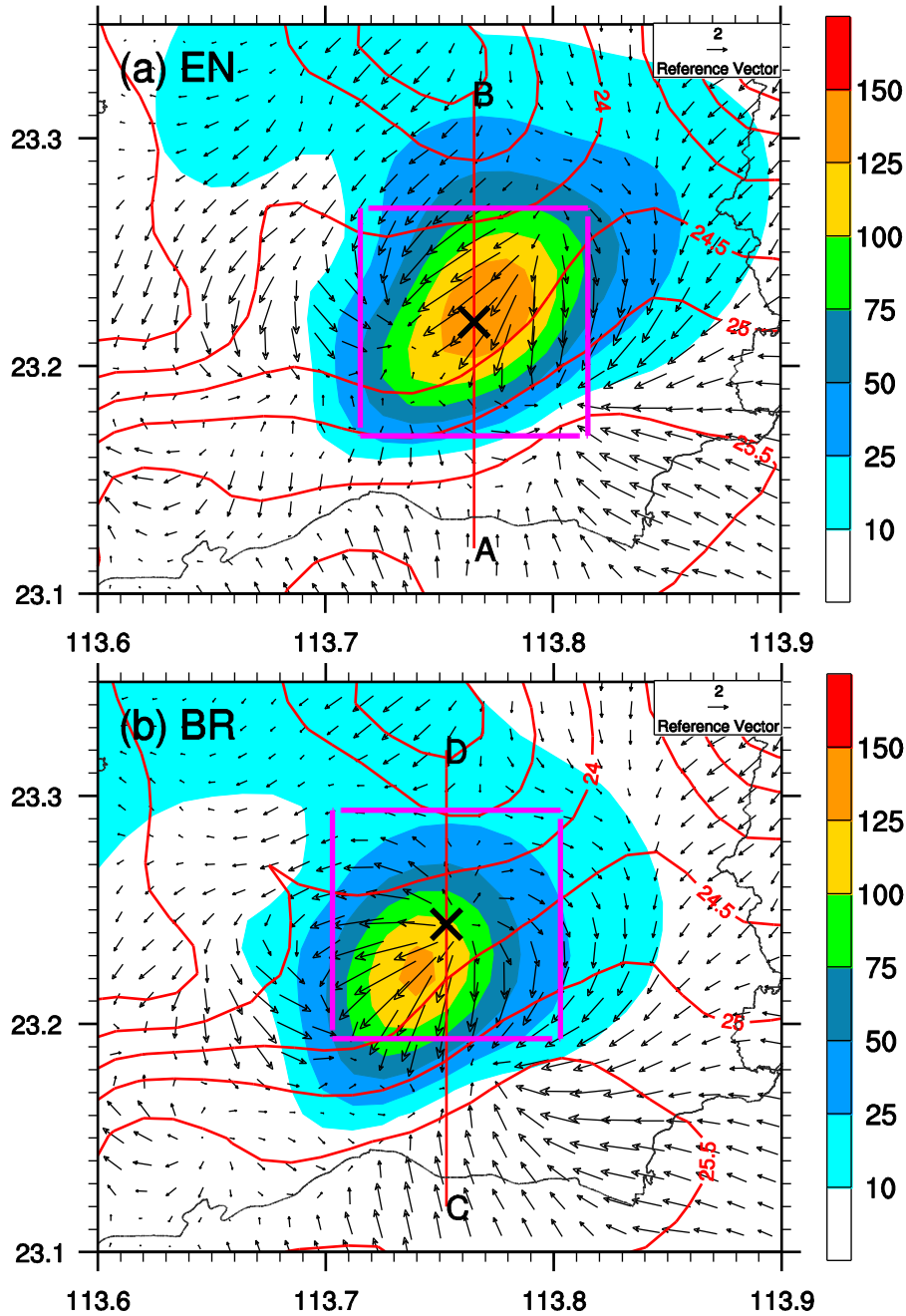
886
887

888 **Fig. 4** Time series of hourly rainfall rates (mm hr⁻¹) from rain gauge observations
 889 (asterisks) and simulated with the EN scheme (circles) and the BR scheme (dots) near
 890 Jiulong during the period of 2000 BST 6 - 1400 BST 7 May 2017. (see Fig. 3 for their
 891 locations)



892

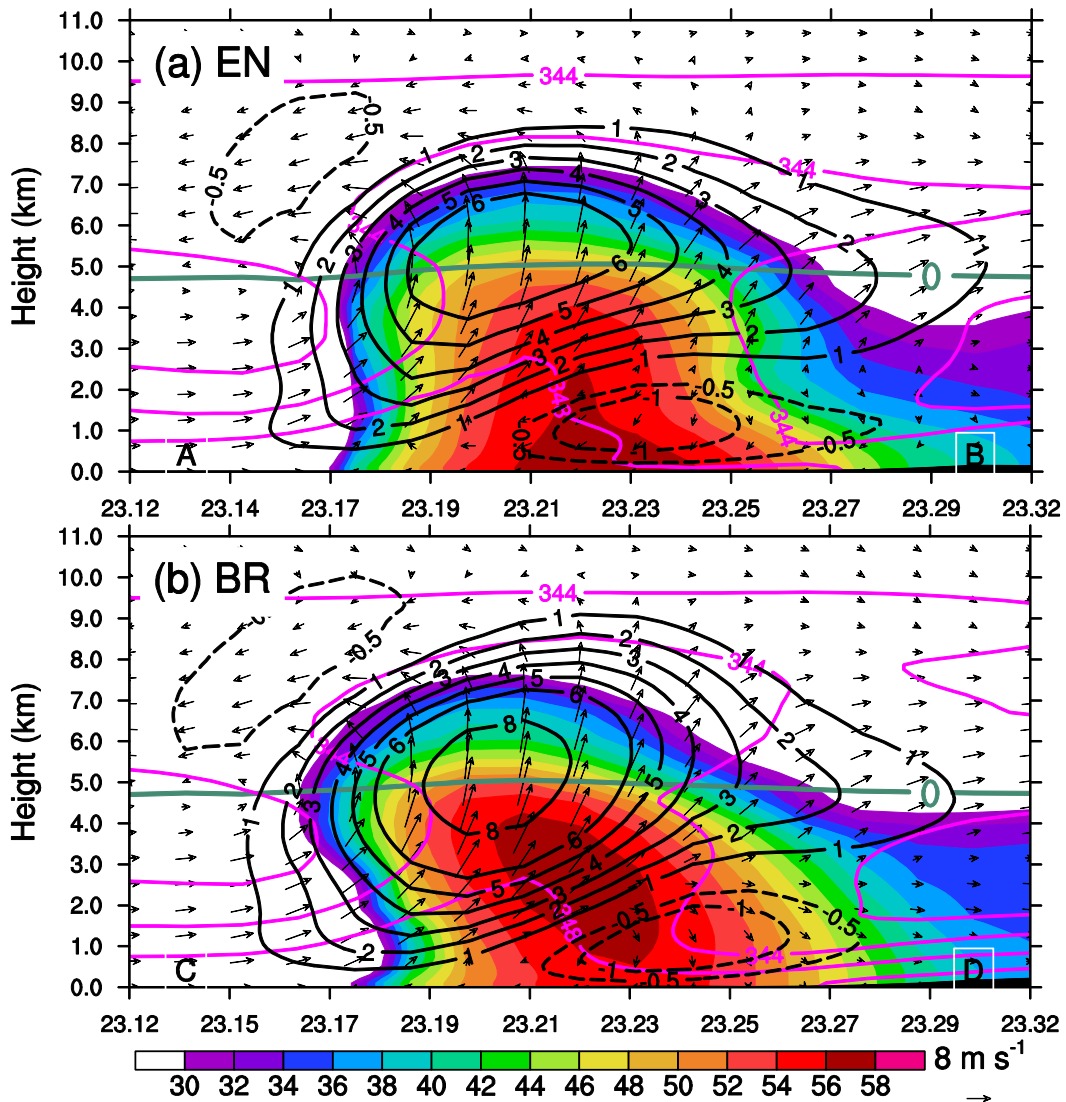
893 **Fig. 5** Horizontal maps of composite radar reflectivity (dBZ, shadings) and surface
 894 ($z = 10$ m) horizontal wind vectors and equivalent potential temperature (θ_e , contoured
 895 at 2K intervals) during the extreme rainfall stage: (a-c) observed, (d-f) simulated with
 896 the EN scheme, and (g-i) simulated with the BR scheme. A reference wind vector is
 897 given beneath the right column next to the composite radar reflectivity color scale.



898

899

900 **Fig. 6** Spatial distribution of hourly rainfall amount (mm, shadings), temporal
 901 -averaged surface temperature (contoured at 0.5°C intervals) and horizontal
 902 wind fields (vectors) during the period from 0600 BST to 0700 BST 7 May, 2017. The red
 903 lines, A-B and C-D, indicate the locations of the vertical cross section in Fig. 7. The
 904 two pink-squared boxes, covering an area of $0.1^\circ \times 0.1^\circ$ with the center of the
 905 maximum hourly rainfall, are marked for domain-averaged in Fig. 8 and Fig. 9.



906

907

908

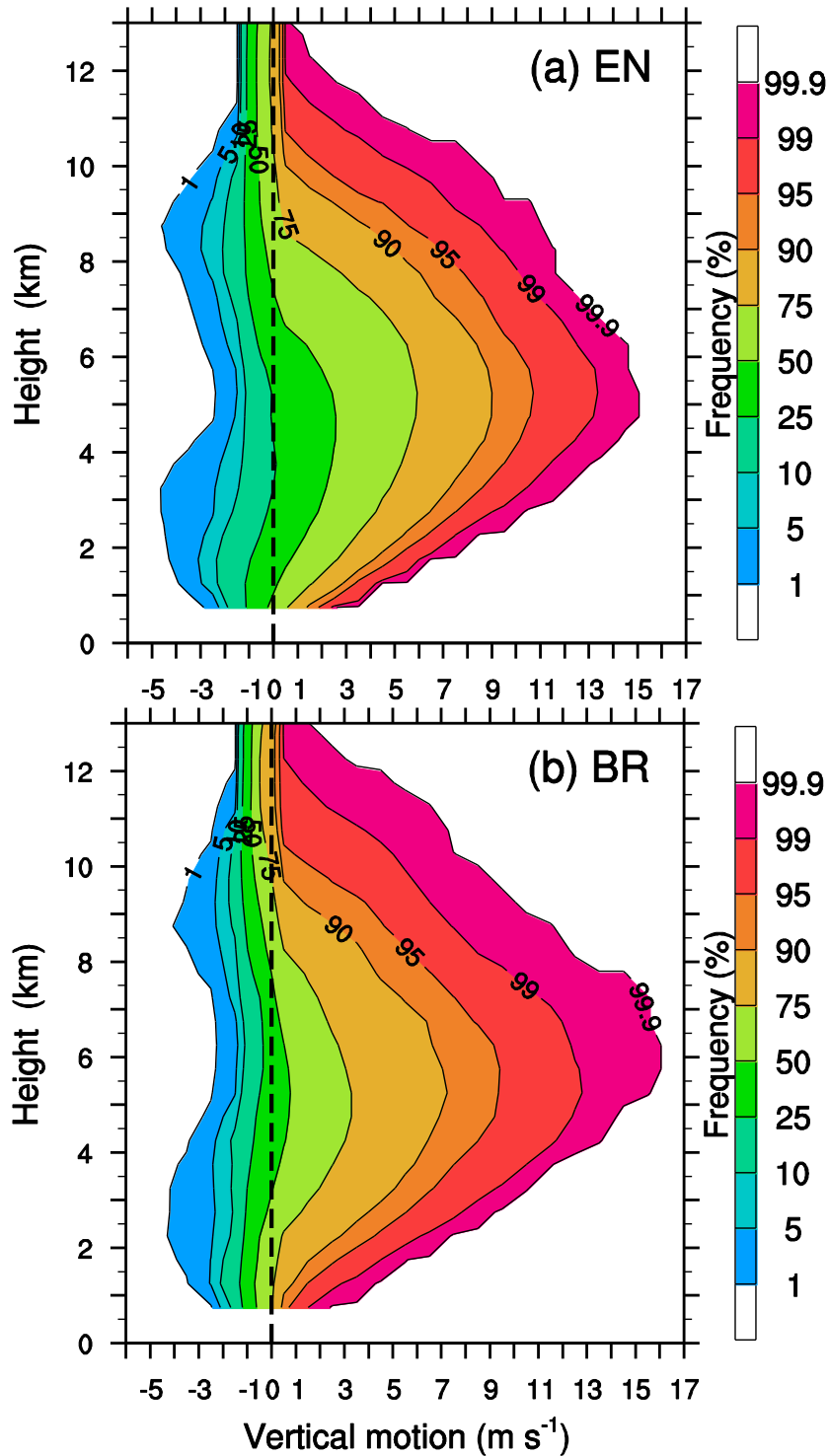
909

910

911

912

Fig. 7 Temporal-averaged vertical cross sections along (a) A-B and (b) C-D in Fig. 6 of the simulated reflectivity (dBZ, shadings), vertical velocity (black contours, m s^{-1}), in-plane flow vectors (vertical motion amplified by a factor of 2), and theta-e (θ_e , pink-contoured at 4K intervals) during the period from 0600 BST to 0700 BST 7 May, 2017. Thick light green line indicates an isotherm of 0°C .



913

914

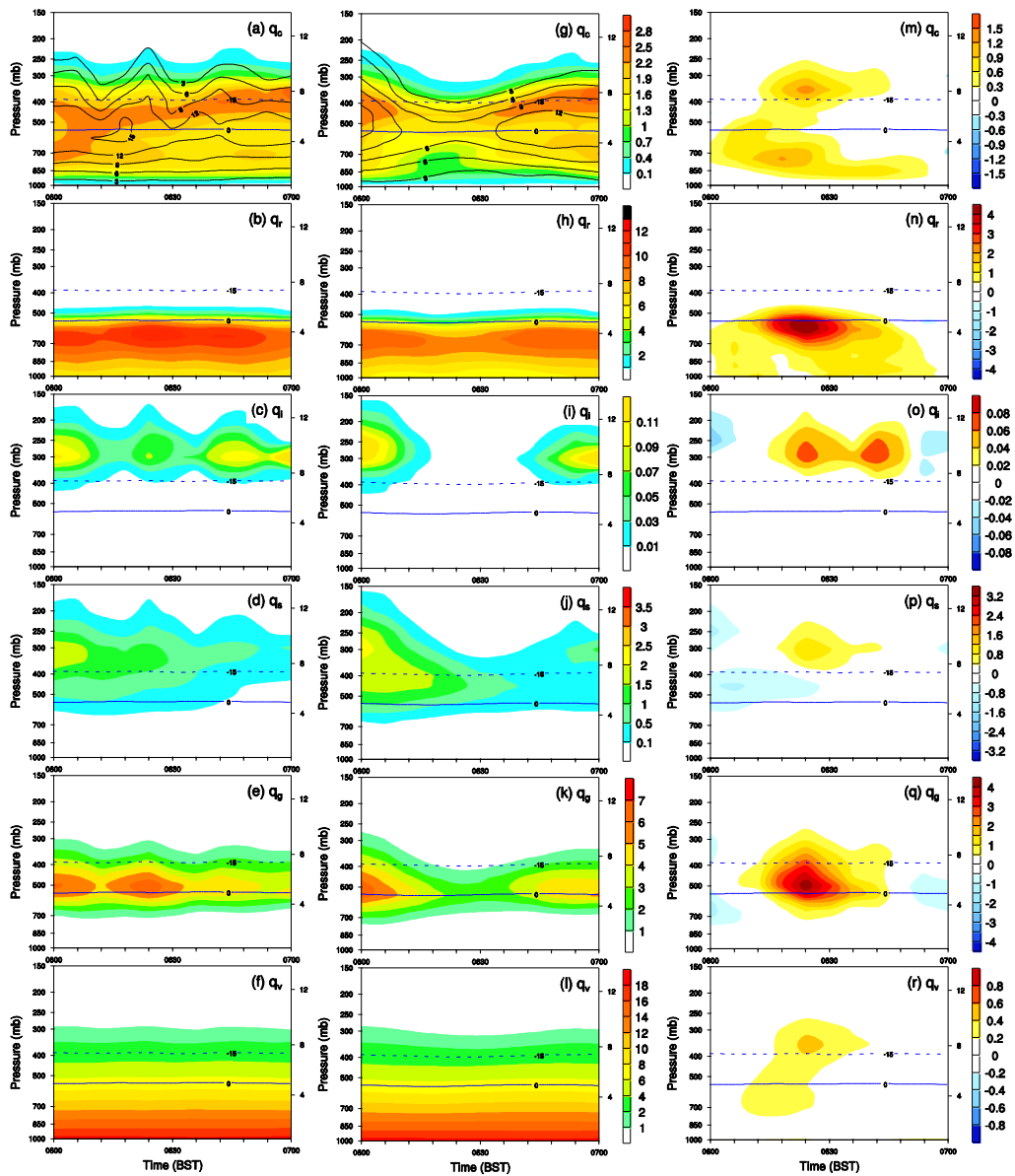
915

916

917

918

Fig. 8 CCFADs of the simulated vertical motion for (a) the EN scheme and (b) the BR scheme within the respective boxes marked with pink lines in Fig. 6. The CCFADs are calculated from eleven model outputs with six-minute intervals during the severe rainfall episode from 0600 BST to 0700 BST 7 May, 2017.



919

920 **Fig. 9** Comparison of time-height cross sections of domain-averaged mixing ratios
 921 between the EN scheme (a-f) and the BR scheme (g-i) during the period from 0600
 922 BST to 0700 BST 7 May, 2017, within the domains marked with pink lines in Fig. 6.
 923 q_c , q_r , q_i , q_s , and q_g denotes cloud water, rainwater, cloud ice, snow, and graupel,
 924 respectively. (m-r) gives the differences between EN and BR (i.e., EN – BR). Thick
 925 blue lines indicate isotherm of -15°C and 0°C , respectively.